Structural insights into Cullin4-RING ubiquitin ligase remodelling by Vpr from simian immunodeficiency viruses

Sofia Banchenko[1¶], Ferdinand Krupp[1¶], Christine Gotthold[1], Jörg Bürger[1,2], Andrea Graziadei[3], Francis O'Reilly[3], Ludwig Sinn[3], Olga Ruda[1], Juri Rappsilber[3,4], Christian M. T. Spahn[1], Thorsten Mielke[2], Ian A. Taylor[5], David Schwefel[1*]

[1] Institute of Medical Physics and Biophysics, Charité – Universitätsmedizin Berlin, corporate member of Freie Universität Berlin, Humboldt-Universität zu Berlin, and Berlin Institute of Health, Berlin, Germany

[2] Microscopy and Cryo-Electron Microscopy Service Group, Max-Planck-Institute for Molecular Genetics, Berlin, Germany

[3] Bioanalytics Unit, Institute of Biotechnology, Technische Universität Berlin, Berlin, Germany

[4] Wellcome Centre for Cell Biology, University of Edinburgh, Edinburgh, United Kingdom

[5] Macromolecular Structure Laboratory, The Francis Crick Institute, London, United Kingdom

*Corresponding author

E-mail: david.schwefel@charite.de (DS)

[¶]These authors contributed equally to this work

Abstract

Viruses have evolved means to manipulate the host's ubiquitin-proteasome system, in order to down-regulate antiviral host factors. The Vpx/Vpr family of lentiviral accessory proteins usurp the substrate receptor DCAF1 of host Cullin4-RING ligases (CRL4), a family of modular ubiquitin ligases involved in DNA replication, DNA repair and cell cycle regulation. $CRL4^{DCAF1}$ specificity modulation by Vpx and Vpr from certain simian immunodeficiency viruses (SIV) leads to recruitment, poly-ubiquitylation and subsequent proteasomal degradation of the host restriction factor SAMHD1, resulting in enhanced virus replication in differentiated cells. To unravel the mechanism of SIV Vpr-induced SAMHD1 ubiquitylation, we conducted integrative biochemical and structural analyses of the Vpr protein from SIVs infecting *Cercopithecus cephus* (SIV_{mus}). X-ray crystallography reveals commonalities between SIV_{mus} Vpr and other members of the Vpx/Vpr family with regard to DCAF1 interaction, while cryo-electron microscopy and cross-linking mass spectrometry highlight a divergent molecular mechanism of SAMHD1 recruitment. In addition, these studies demonstrate how SIV_{mus} Vpr exploits the dynamic architecture of the multi-subunit $CRL4^{DCAF1}$ assembly to optimise SAMHD1 ubiquitylation. Together, the present work provides detailed molecular insight into variability and species-specificity of the evolutionary arms race between host SAMHD1 restriction and lentiviral counteraction through Vpx/Vpr proteins.

Author summary

Due to the limited size of virus genomes, virus replication critically relies on host cell components. In addition to the host cell's energy metabolism and its DNA replication and protein synthesis apparatus, the protein degradation machinery is an attractive target for viral re-appropriation. Certain viral factors divert the specificity of host ubiquitin ligases to antiviral host factors, in order to mark them for destruction by the proteasome, to lift intracellular barriers to virus replication. Here, we present molecular details of how the simian immunodeficiency virus accessory protein Vpr interacts with a substrate receptor of host Cullin4-RING ubiquitin ligases, and how this interaction redirects the specificity of Cullin4-RING to the antiviral host factor SAMHD1. The studies uncover the mechanism of Vpr-induced SAMHD1 recruitment and subsequent ubiquitylation. Moreover, by comparison to related accessory proteins from other immunodeficiency virus species, we illustrate the surprising variability in the molecular strategies of SAMHD1 counteraction, which these viruses adopted during evolutionary adaptation to their hosts. Lastly, our work also provides deeper insight into the inner workings of the host's Cullin4-RING ubiquitylation machinery.

Introduction

A large proportion of viruses have evolved means to co-opt their host's ubiquitylation machinery, in order to improve replication conditions, either by introducing viral ubiquitin ligases and deubiquitinases, or by modification of host proteins involved in ubiquitylation [1-3]. In particular, host ubiquitin ligases are a prominent target for viral usurpation, to redirect specificity towards antiviral host restriction factors. This results in recruitment of restriction factors as non-endogenous *neo*-substrates, inducing their poly-ubiquitylation and subsequent proteasomal degradation [4-8]. This counteraction of the host's antiviral repertoire is essential for virus infectivity and spread [9-12], and mechanistic insights into these specificity changes extend our understanding of viral pathogenesis and might pave the way for novel treatments.

Frequently, virally encoded modifying proteins associate with, and adapt the Cullin4-RING ubiquitin ligases (CRL4) [5]. CRL4 consists of a Cullin4 (CUL4) scaffold that bridges the catalytic RING-domain subunit ROC1 to the adaptor protein DDB1, which in turn binds to exchangeable substrate receptors (DCAFs, DDB1- and CUL4-associated factors) [13-17]. In some instances, the DDB1 adaptor serves as an anchor for virus proteins, which then act as "viral DCAFs" to recruit the antiviral substrate. Examples are the simian virus 5 V protein and mouse cytomegalovirus M27, which bind to DDB1 and recruit STAT1/2 proteins for ubiquitylation, in order to interfere with the host's interferon response [18-20]. Similarly, CUL4-dependent downregulation of STAT signalling is important for West Nile Virus replication [21]. In addition, the hepatitis B virus X protein hijacks DDB1 to induce proteasomal destruction of the structural maintenance of chromosome (SMC) complex to promote virus replication [22, 23].

Viral factors also bind to and modify DCAF receptors in order to redirect them to antiviral substrates. Prime examples are the lentiviral accessory proteins Vpr and Vpx. All contemporary human and simian immunodeficiency viruses (HIV/SIV) encode Vpr, while only two lineages, represented by HIV-2 and SIV infecting mandrills, carry Vpx [24]. Vpr and Vpx proteins are packaged into progeny virions and released into the host cell upon infection, where they bind to DCAF1 in the nucleus [25]. In this work, corresponding simian immunodeficiency virus Vpx/Vpr proteins will be indicated with their host species as subscript, with the following abbreviations used: mus – moustached monkey (*Cercopithecus*

cephus), mnd – mandrill (*Mandrillus sphinx*), rcm – red-capped mangabey (*Cercocebus torquatus*), sm – sooty mangabey (*Cercocebus atys*), deb – De Brazza's monkey (*Cercopithecus neglectus*), syk – Syke's monkey (*Cercopithecus albogularis*), agm – african green monkey (*Chlorocebus* spec).

Vpr_{HIV-1} is important for virus replication *in vivo* and in macrophage infection models [26]. Recent proteomic analyses revealed that DCAF1 specificity modulation by Vpr_{HIV-1} proteins results in down-regulation of hundreds of host proteins in a DCAF1- and proteasome-dependent manner [27], including the previously reported Vpr_{HIV-1} degradation targets UNG2 [28], HLTF [29], MUS81 [30, 31], MCM10 [32] and TET2 [33]. This surprising promiscuity in degradation targets is also partially conserved in more distant clades exemplified by Vpr_{agm} and Vpr_{mus} [27]. However, Vpr pleiotropy, and the lack of easily accessible experimental models, have prevented a characterisation of how these degradation events precisely promote replication [26].

By contrast, Vpx, exhibits a much narrower substrate range. It has recently been reported to target stimulator of interferon genes (STING) and components of the human silencing hub (HUSH) complex for degradation, leading to inhibition of antiviral cGAS-STING-mediated signalling and reactivation of latent proviruses, respectively [34-36]. Importantly, Vpx also recruits the SAMHD1 restriction factor to DCAF1, in order to mark it for proteasomal destruction [37, 38]. SAMHD1 is a deoxynucleotide triphosphate (dNTP) triphosphohydrolase that restricts retroviral replication in non-dividing cells by lowering the dNTP pool to levels that cannot sustain viral reverse transcription [39-46]. Retroviruses that express Vpx are able to alleviate SAMHD1 restriction and allow replication in differentiated myeloid lineage cells, resting T cells and memory T cells [38, 47, 48]. As a result of the constant evolutionary arms race between the host's SAMHD1 restriction and its viral antagonist Vpx, the mechanism of Vpx-mediated SAMHD1 recruitment is highly virus species- and strain-specific: The Vpx clade represented by Vpx_{HIV-2} recognises the SAMHD1 C-terminal domain (CtD), while $Vpx_{mnd2/rcm}$ binds the SAMHD1 N-terminal domain (NtD) in a fundamentally different way [24, 49-52].

In the course of evolutionary adaptation to their primate hosts, and due to selective pressure to evade SAMHD1 restriction, two groups of SIVs that do not have Vpx, SIV_{agm}, and $SIV_{deb/mus/syk}$, *neo*-functionalised their Vpr to bind SAMHD1 and induce its degradation [24, 49, 53]. Consequently, these

107 species evolved "hybrid" Vpr proteins that retain targeting of some host factors depleted by HIV-1-type
108 Vpr [27], and additionally induce SAMHD1 degradation.
109 To uncover the molecular mechanisms of DCAF1- and SAMHD1-interaction of such a "hybrid" Vpr,
110 we initiated integrative biochemical and structural analyses of the Vpr protein from an SIV infecting
111 *Cercopithecus cephus*, Vpr_{mus}. These studies reveal similarities and differences to Vpx and Vpr proteins
112 from other lentivirus species and pinpoint the divergent molecular mechanism of Vpr_{mus}-dependent
113 SAMHD1 recruitment to $CRL4^{DCAF1}$. Furthermore, cryo-electron microscopic (cryo-EM)
114 reconstructions of a Vpr_{mus}-modified $CRL4^{DCAF1}$ protein complex allow for insights into the structural
115 plasticity of the entire CRL4 ubiquitin ligase assembly, with implications for the ubiquitin transfer
116 mechanism.
117

118 # Results

119 ## SAMHD1-CtD is necessary and sufficient for Vpr_{mus}-binding and ubiquitylation in vitro

120 To investigate the molecular interactions between Vpr_{mus}, the *neo*-substrate SAMHD1 from rhesus
121 macaque and CRL4 subunits DDB1/DCAF1 C-terminal domain (DCAF1-CtD), protein complexes were
122 reconstituted *in vitro* from purified components and analysed by gel filtration (GF) chromatography.
123 The different protein constructs that were employed are shown schematically in S1A Fig. Vpr_{mus} is
124 insoluble after removal of the GST affinity purification tag (S1B Fig) and accordingly could not be
125 applied to the GF column. No interaction of SAMHD1 with DDB1/DCAF1-CtD could be detected in
126 the absence of Vpr_{mus} (S1C Fig). Analysis of binary protein combinations (Vpr_{mus} and DDB1/DCAF1-
127 CtD; Vpr_{mus} and SAMHD1) shows that Vpr_{mus} elutes in a single peak together with DDB1/DCAF1-CtD
128 (S1D Fig) or with SAMHD1 (S1E Fig). Incubation of Vpr_{mus} with DDB1/DCAF1B and SAMHD1
129 followed by GF resulted in elution of all three components in a single peak (Fig 1A, B, red trace).
130 Together, these results show that Vpr_{mus} forms stable binary and ternary protein complexes with
131 DDB1/DCAF1-CtD and/or SAMHD1 *in vitro*. Furthermore, incubation with any of these interaction
132 partners apparently stabilises Vpr_{mus} by alleviating its tendency for aggregation/insolubility.
133 Previous cell-based assays indicated that residues 583-626 of rhesus macaque SAMHD1 (SAMHD1-
134 CtD) are necessary for Vpr_{mus}-induced proteasomal degradation [49]. To test this finding in our *in vitro*

system, constructs containing SAMHD1-CtD fused to T4 lysozyme (T4L-SAMHD1-CtD), or lacking SAMHD1-CtD (SAMHD1-ΔCtD, Fig 1A), were incubated with Vpr_{mus} and DDB1/DCAF1-CtD, and complex formation was assessed by GF chromatography. Analysis of the resulting chromatograms by SDS-PAGE shows that SAMHD1-ΔCtD did not co-elute with DDB1/DCAF1-CtD/Vpr_{mus} (Fig 1A, B, green trace). By contrast, T4L-SAMHD1-CtD accumulated in a single peak, which also contained DDB1/DCAF1-CtD and Vpr_{mus} (Fig 1A, B, cyan trace). These results confirm that SAMHD1-CtD is necessary for stable association with DDB1/DCAF1-CtD/Vpr_{mus} *in vitro*, and demonstrate that SAMHD1-CtD is sufficient for Vpr_{mus}-mediated recruitment of the T4L-SAMHD1-CtD fusion construct to DDB1/DCAF1-CtD.

To correlate these data with enzymatic activity, *in vitro* ubiquitylation assays were conducted by incubating SAMHD1, SAMHD1-ΔCtD or T4L-SAMHD1-CtD with purified $CRL4^{DCAF1\text{-}CtD}$, E1 (UBA1), E2 (UBCH5C), ubiquitin and ATP. Input proteins are shown in S2A Fig, and control reactions in S2B, C Fig. In the absence of Vpr_{mus}, no SAMHD1 ubiquitylation was observed (Figs 1C and S2D), while addition of Vpr_{mus} resulted in robust SAMHD1 ubiquitylation (Figs 1D and S2E). In agreement with the analytical GF data, SAMHD1-ΔCtD was not ubiquitylated in the presence of Vpr_{mus} (Figs 1E and S2F), while T4L-SAMHD1-CtD, was ubiquitylated with similar kinetics as the full-length protein (Figs 1F and S2F). Again, these data substantiate the functional importance of SAMHD1-CtD for Vpr_{mus}-mediated recruitment to the $CRL4^{DCAF1}$ ubiquitin ligase.

Crystal Structure analysis of apo- and Vpr_{mus}-bound DDB1/DCAF1-CtD protein complexes

To obtain structural information regarding Vpr_{mus} and its mode of binding to the CRL4 substrate receptor DCAF1, the X-ray crystal structures of a DDB1/DCAF1-CtD complex, and DDB1/DCAF1-CtD/T4L-Vpr_{mus} (residues 1-92) fusion protein ternary complex were determined. The structures were solved using molecular replacement and refined to resolutions of 3.1 Å and 2.5 Å respectively (S1 Table). Vpr_{mus} adopts a three-helix bundle fold, stabilised by coordination of a zinc ion by His and Cys residues on Helix-1 and at the C-terminus (Fig 2A). Superposition of Vpr_{mus} with previously determined Vpx_{sm} [50], Vpx_{mnd2} [51, 52], and $Vpr_{HIV\text{-}1}$ [54] structures reveals a conserved three-helix bundle fold, and

similar position of the helix bundles on DCAF1-CtD (S3A Fig). In addition, the majority of side chains involved in DCAF1-interaction are type-conserved in all Vpx and Vpr proteins (Figs S3B-G and S6A), strongly suggesting a common molecular mechanism of host CRL4-DCAF1 hijacking by the Vpx/Vpr family of accessory proteins. However, there are also significant differences in helix length and register as well as conformational variation in the loop region N-terminal of Helix-1, at the start of Helix-1 and in the loop between Helices-2 and -3 (S3A Fig).

Vpr_{mus} binds to the side and on top of the disk-shaped 7-bladed β-propeller (BP) DCAF1-CtD domain with a total contact surface area of ~1600 $Å^2$ comprising three major regions of interaction. The extended Vpr_{mus} N-terminus attaches to the cleft between DCAF1 BP blades 1 and 2 through several hydrogen bonds, electrostatic and hydrophobic interactions (S3B-D Fig). A second, smaller contact area is formed by hydrophobic interaction between Vpr_{mus} residues L31 and E34 from Helix-1, and DCAF1 W1156, located in a loop on top of BP blade 2 (S3E Fig). The third interaction surface comprises the C-terminal half of Vpr_{mus} Helix-3, which inserts into a ridge on top of DCAF1 (S3F, G Fig).

Superposition of the apo-DDB1/DCAF1-CtD and Vpr_{mus}-bound crystal structures reveals conformational changes in DCAF1 upon Vpr_{mus} association. Binding of the N-terminal arm of Vpr_{mus} induces only a minor rearrangement of a loop in BP blade 2 (S3C Fig). By contrast, significant structural changes occur on the upper surface of the BP domain: polar and hydrophobic interactions of DCAF1 residues P1329, F1330, F1355, N1371, L1378, M1380 and T1382 with Vpr_{mus} side chains of T79, R83, R86 and E87 in Helix-3 result in the stabilisation of the sequence stretch that connect BP blades 6 and 7 ("C-terminal loop", Figs 2B and S3F). Moreover, side chain electrostatic interactions of Vpr_{mus} residues R15, R75 and R76 with DCAF1 E1088, E1091 and E1093 lock the conformation of an "acidic loop" upstream of BP blade 1, which is also unstructured and flexible in the absence of Vpr_{mus} (Figs 2B, C and S3D, F).

Notably, in previously determined structures of Vpx/DCAF1/SAMHD1 complexes the "acidic loop" is a central point of ternary contact, providing a binding platform for positively charged amino acid side chains in either the SAMHD1 N- or C-terminus [50-52]. For example, Vpx_{sm} positions SAMHD1-CtD in such a way, that SAMHD1 K622 engages in electrostatic interaction with the DCAF1 "acidic loop" residue D1092 (Fig 2C, left panel). However, in the Vpr_{mus} crystal structure the bound Vpr_{mus} now blocks

191 access to the corresponding SAMHD1-CtD binding pocket, in particular by the positioning of an
192 extended N-terminal loop that precedes Helix-1. Additionally, Vpr_{mus} side chains R15, R75 and R76
193 neutralise the DCAF1 "acidic loop", precluding the formation of further salt bridges to basic residues in
194 SAMHD1-CtD (Fig 2C, right panel).
195 To validate the importance of Vpr_{mus} residues R15 and R75 for DCAF1-CtD- and SAMHD1-binding,
196 charge reversal mutations to glutamates were generated by site-directed mutagenesis. The effect of the
197 Vpr_{mus} R15E R75E double mutant on complex assembly was then analysed by GF chromatography.
198 SDS-PAGE analysis of the resulting chromatographic profile shows an almost complete loss of the
199 DDB1/DCAF1-CtD/Vpr_{mus}/SAMHD1 complex peak (Fig 2D, fraction 6), when compared to the wild
200 type, concomitant with enrichment of (i) Vpr_{mus} R15E R75E-bound DDB1/DCAF1-CtD (Fig 2D,
201 fractions 7-8), and of (ii) Vpr_{mus} R15E R75E/SAMHD1 binary complex (Fig 2D, fraction 8-9). This
202 suggests that charge reversal of Vpr_{mus} side chains R15 and R75 weakens the strong association with
203 DCAF1 observed in wild type Vpr_{mus}, due to loss of electrostatic interaction with the "acidic loop", in
204 accordance with the crystal structure. Consequently, some proportion of Vpr-bound SAMHD1
205 dissociates, further indicating that Vpr_{mus} side chains R15 and R75 are not central to SAMHD1
206 interaction.
207

208 **Molecular mechanism of SAMHD1-targeting**

209 To obtain mechanistic insight into Vpr_{mus}-recruitment of SAMHD1-CtD, we initiated cryo-EM analyses
210 of the $CRL4^{DCAF1\text{-}CtD}$/Vpr_{mus}/SAMHD1 assembly. In these studies, the small ubiquitin-like protein
211 NEDD8 was enzymatically attached to the CUL4 subunit, in order to obtain its active form (S4A Fig)
212 [55]. A CRL4-$NEDD8^{DCAF1\text{-}CtD}$/Vpr_{mus}/SAMHD1 complex was reconstituted *in vitro* and purified by GF
213 chromatography (S4B Fig). Extensive 2D and 3D classification of the resulting particle images revealed
214 considerable conformational heterogeneity, especially regarding the position of the CUL4-
215 NEDD8/ROC1 subcomplex (stalk) relative to DDB1/DCAF1/Vpr_{mus} (core), (S4 Fig).
216 Nevertheless, a homogeneous particle population could be separated, which yielded a 3D reconstruction
217 at a nominal resolution of 7.3 Å that contained electron density corresponding to the core (S4C-F Fig).
218 Molecular models of DDB1 BP domains A and C (BPA, BPC), DCAF1-CtD and Vpr_{mus}, derived from

our crystal structure (Fig 2), could be fitted as rigid bodies into this cryo-EM volume (Fig 3A). No obvious electron density was visible for the bulk of SAMHD1. However, close inspection revealed an additional tubular, slightly arcing density feature, approx. 35 Å in length, located on the upper surface of the Vpr_{mus} helix bundle, approximately 17 Å away from and opposite of the Vpr_{mus}/DCAF1-CtD binding interface (Fig 3A, red arrows). One end of the tubular volume contacts the middle of Vpr_{mus} Helix-1, and the other end forms additional contacts to the C-terminus of Helix-2 and the N-terminus of Helix-3. A local resolution of 7.5-8 Å precluded the fitting of an atomic model. Considering the biochemical data, showing that SAMHD1-CtD is sufficient for recruitment to DDB1/DCAF1/Vpr_{mus}, we hypothesise that this observed electron density feature corresponds to the region of SAMHD1-CtD which physically interacts with Vpr_{mus}. Given its dimensions, the putative SAMHD1-CtD density could accommodate approx. 10 amino acid residues in a fully extended conformation or up to 23 residues in a kinked helical arrangement. All previous crystal structure analyses [46], as well as secondary structure predictions indicate that SAMHD1 residues C-terminal to the catalytic HD domain and C-terminal lobe (amino acids 599-626) are disordered in the absence of additional binding partners. Accordingly, the globular domains of the SAMHD1 molecule might be flexibly linked to the C-terminal tether identified here. In that case, the bulk of SAMHD1 samples a multitude of positions relative to the DDB1/DCAF1-CtD/Vpr_{mus} core, and consequently is averaged out in the process of cryo-EM reconstruction.

The topology of $CRL4^{DCAF1\text{-}CtD}$/Vpr_{mus}/SAMHD1 and the binding region of SAMHD1-CtD were further assessed by cross-linking mass spectrometry (CLMS) using the photo-reactive cross-linker sulfo-SDA [56]. A large number of cross-links between SAMHD1 and the C-terminal half of CUL4, the side and top of DCAF1-CtD, and BP blades 6-7 of DDB1 were found, consistent with highly variable positioning of the SAM and HD domains of SAMHD1 relative to the CRL4 core (Fig 3B). Moreover, multiple cross-links between SAMHD1-CtD and Vpr_{mus} were observed, more specifically locating to a sequence stretch comprising the C-terminal half of Vpr_{mus} Helix-1 (residues A27-E36), and to a portion of the disordered Vpr_{mus} C-terminus (residues Y90, Y100). These data are in accordance with the presence of SAMHD1-CtD in the unassigned cryo-EM density and its role as Vpr_{mus} tether. The remaining SAMHD1-CtD cross-links were with the C-terminus of CUL4 and the “acidic loop” of DCAF1 (Fig 3B). Distance restraints from these SAMHD1-CtD cross-links, together with our structural models of

247 $CRL4^{DCAF1\text{-}CtD}/Vpr_{mus}$ (see below), were employed to visualise the interaction space accessible to the
248 centre of mass of SAMHD1-CtD. This analysis is compatible with recruitment of SAMHD1-CtD on top
249 of the Vpr_{mus} helix bundle as indicated by cryo-EM (Fig 3C). Interestingly, cross-links to Vpr_{mus} were
250 restricted to the C-terminal end of SAMHD1-CtD (residues K622, K626), while cross-links to CUL4
251 and DCAF1 were found in the N-terminal portion (residues K595, K596, T602-S606). These
252 observations are consistent with a model where the very C-terminus of SAMHD1 is immobilised on
253 Vpr_{mus}, and SAMHD1-CtD residues further upstream are exposed to the catalytic machinery
254 surrounding the CUL4 C-terminal domain.
255 To further probe the interaction, Vpr_{mus} amino acid residues in close proximity to the putative SAMHD1-
256 CtD density were substituted by site-directed mutagenesis. Specifically, Vpr_{mus} W29 was changed to
257 alanine to block a hydrophobic contact with SAMHD1-CtD involving the aromatic side chain, and
258 Vpr_{mus} A66 was changed to a bulky tryptophan, in order to introduce a steric clash with SAMHD1-CtD
259 (Fig 3D). This Vpr_{mus} W29A A66W double mutant was then assessed for complex formation with
260 DDB1/DCAF1-CtD and SAMHD1 by analytical GF. In comparison to wild type Vpr_{mus}, the W29A
261 A66W mutant showed a reduction of DDB1/DCAF1-CtD/Vpr_{mus}/SAMHD1 complex peak intensity (Fig
262 3E, fraction 6), concomitant with (i) enrichment of DDB1/DCAF1-CtD/Vpr_{mus} ternary complex, sub-
263 stoichiometrically bound to SAMHD1 (Fig 3E, fraction 7), (ii) excess DDB1/DCAF1-CtD binary
264 complex (Fig 3E, fraction 8), and (iii) monomeric SAMHD1 species (Fig 3E, fractions 9-10). In
265 conclusion, this biochemical analysis, together with cryo-EM reconstruction at intermediate resolution
266 and CLMS analysis, locate the SAMHD1-CtD binding site on the upper surface of the Vpr_{mus} helix
267 bundle.
268 These data allow for structural comparison with *neo*-substrate binding modes of Vpx and Vpr proteins
269 from different retrovirus lineages (Fig 4A-D). $Vpx_{HIV\text{-}2}$ and Vpx_{sm} position SAMHD1-CtD at the side of
270 the DCAF1 BP domain through interactions with the N-termini of Vpx Helices-1 and -3 (Fig 4B) [50].
271 Vpx_{mnd2} and Vpx_{rcm} bind SAMHD1-NtD using a bipartite interface comprising the side of the DCAF1
272 BP and the upper surface of the Vpx helix bundle (Fig 4C) [51, 52]. $Vpr_{HIV\text{-}1}$ engages its ubiquitylation
273 substrate UNG2 using both the top and the upper edge of the $Vpr_{HIV\text{-}1}$ helix bundle (Fig 4D) [54]. Of
274 note, these upper-surface interaction interfaces only partially overlap with the Vpr_{mus}/SAMHD1-CtD

binding interface identified here and employ fundamentally different sets of interacting amino acid residues. Thus, it appears that the molecular interaction interfaces driving Vpx/Vpr-mediated *neo*-substrate recognition and degradation are not conserved between related SIV and HIV Vpx/Vpr accessory proteins, even in cases where identical SAMHD1-CtD regions are targeted for recruitment.

Cryo-EM analysis of Vpr_{mus}-modified CRL4-NEDD8$^{DCAF1\text{-}CtD}$ conformational states and dynamics

A reanalysis of the cryo-EM data using strict selection of high-quality 2D classes, followed by focussed 3D classification yielded three additional particle populations, resulting in 3D reconstructions at 8-10 Å resolution, which contained both the Vpr_{mus}-bound CRL4 core and the stalk (conformational states-1, -2 and -3, Figs 5A and S4G-J). The quality of the 3D volumes was sufficient to fit crystallographic models of core (Fig 2) and the stalk (PDB 2hye) [15] as rigid bodies (Figs 5B and S5A). For the catalytic RING-domain subunit ROC1, only fragmented electron density was present near the position it occupies in the crystallographic model (S5A Fig). In all three states, electron density was selectively absent for the C-terminal CUL4 winged helix B (WHB) domain (residues 674-759), which contains the NEDD8 modification site (K705), and for the preceding α-helix, which connects the CUL4 N-terminal domain to the WHB domain (S5A Fig). In accordance with this observation, the positions of CRL5-attached NEDD8 and of the CRL4 ROC1 RING domain are sterically incompatible upon superposition of their respective crystal structures (S5B Fig) [57].

Alignment of 3D volumes from states-1, -2 and -3 shows that core densities representing DDB1 BPA, BPC, DCAF1-CtD and Vpr_{mus} superimpose well, indicating that these components do not undergo major conformational fluctuations and thus form a rigid platform for substrate binding and attachment of the CRL4 stalk (Fig 5). However, rotation of DDB1 BPB around a hinge connecting it to BPC results in three different orientations of state-1, -2 and -3 stalk regions relative to the core. BPB rotation angles were measured as 69° between state-1 and -2, and 50° between state-2 and -3. Furthermore, the crosslinks between DDB1 and CUL4 identified by CLMS are satisfied by the state-1 model, but increasingly violated in states-2 and -3, validating in solution the conformational variability observed by cryo-EM. (S5C Fig). Taken together, this places the CRL4 catalytic machinery, sited at the distal end

of the stalk, appropriately to approach the Vpr_{mus}-tethered bulk of SAMHD1 for ubiquitylation at a wide range of angles (Fig 5B).

These data are in line with previous prediction based on extensive comparative crystal structure analyses, which postulated an approx. 150° rotation of the CRL4 stalk around the core [13, 15, 16, 19, 58]. However, the left- and rightmost CUL4 orientations observed here, states-1 and -3 from our cryo-EM analysis, indicate a slightly narrower stalk rotation range (119°), when compared to the outermost stalk conformations modelled from previously determined crystal structures (143°) (S5D Fig). An explanation for this discrepancy comes from inspection of the cryo-EM densities and fitted models, revealing that along with the main interaction interface on DDB1 BPB there are additional molecular contacts between CUL4 and DDB1. Specifically, in state-1, there is a contact between the loop connecting helices D and E of CUL4 cullin repeat (CR)1 (residues 161-169) and a loop protruding from BP blade 3 of DDB1 BPC (residues 795-801, S5E Fig). In state-3, the loop between CUL4 CR2 helices D and E (residues 275-282) abuts a region in the C-terminal helical domain of DDB1 (residues 1110-1127, S5F Fig). These auxiliary interactions might be required to lock the outermost stalk positions observed here in order to confine the rotation range of CUL4.

Discussion

Our X-ray crystallographic studies of the DDB1/DCAF1-CtD/Vpr_{mus} assembly provide the first structural insight into a class of "hybrid" SIV Vpr proteins. These are present in the SIV_{agm} and $SIV_{mus/deb/syk}$ lineages of lentiviruses and combine characteristics of related Vpr_{HIV-1} and SIV Vpx accessory proteins.

Like SIV Vpx, "hybrid" Vpr proteins down-regulate the host restriction factor SAMHD1 by recruiting it to $CRL4^{DCAF1}$ for ubiquitylation and subsequent proteasomal degradation. However, using a combination of X-ray, cryo-EM and CLMS analyses, we show that the molecular strategy, which Vpr_{mus} evolved to target SAMHD1, is strikingly different from Vpx-containing SIV strains. In the two clades of Vpx proteins, divergent amino acid sequence stretches just upstream of Helix-1 (variable region (VR)1, S6A Fig), together with polymorphisms in the SAMHD1-N-terminus of the respective host species, determine if HIV-2-type or SIV_{mnd}-type Vpx recognise SAMHD1-CtD or SAMHD1-NtD,

respectively. These recognition mechanisms result in positioning of SAMHD1-CtD or -NtD on the side of the DCAF1 BP domain in a way that allows for additional contacts between SAMHD1 and DCAF1, thus forming ternary Vpx/SAMHD1/DCAF1 assemblies with very low dissociation rates [50-52, 59]. In Vpr_{mus}, different principles determine the specificity for SAMHD1-CtD. Here, VR1 is not involved in SAMHD1-CtD-binding at all, but forms additional interactions with DCAF1, which are not observed in Vpx/DCAF1 protein complexes (S6A Fig). Molecular contacts between Vpr_{mus} and SAMHD1 are dispersed on Helices-1 and -3, facing away from the DCAF1 interaction site and immobilising SAMHD1-CtD on the top side of the Vpr_{mus} helix bundle (S6A Fig). Placement of SAMHD1-CtD in such a position precludes stabilising ternary interaction with DCAF1-CtD, but still results in robust SAMHD1 ubiquitylation *in vitro* and SAMHD1 degradation in cell-based assays [24].

Predictions regarding the molecular mechanism of SAMHD1-binding by other "hybrid" Vpr orthologues are difficult due to sequence divergence. Even in Vpr_{deb}, the closest relative to Vpr_{mus}, only approximately 50% of amino acid side chains lining the putative SAMHD1-CtD binding pocket are conserved (S6A Fig). Previous *in vitro* ubiquitylation and cell-based degradation experiments did not show a clear preference of Vpr_{deb} for recruitment of either SAMHD1-NtD or –CtD [24, 49]. Furthermore, it is disputed if Vpr_{deb} actually binds DCAF1 [60], which might possibly be explained by amino acid variations in the very N-terminus and/or in Helix-3 (S6A Fig). Vpr_{syk} is specific for SAMHD1-CtD [49], but the majority of residues forming the binding platform for SAMHD1-CtD observed in the present study are not conserved. The SIV_{agm} lineage of Vpr proteins is even more divergent, with significant differences not only in possible SAMHD1-contacting residues, but also in the sequence stretches preceding Helix-1, and connecting Helices-2 and -3, as well as in the N-terminal half of Helix-3 (S6A Fig). Furthermore, there are indications that recruitment of SAMHD1 by the $Vpr_{agm.GRI}$ sub-type involves molecular recognition of both SAMHD1-NtD and –CtD [49, 53]. In conclusion, recurring rounds of evolutionary lentiviral adaptation to the host SAMHD1 restriction factor, followed by host re-adaptation, resulted in highly species-specific, diverse molecular modes of Vpr-SAMHD1 interaction. In addition to the example presented here, further structural characterisation of SAMHD1-Vpr complexes will be necessary to illustrate the manifold outcomes of this particular virus-host molecular "arms race".

Previous structural investigation of DDB1/DCAF1/Vpr_{HIV-1} in complex with the *neo*-substrate UNG2 demonstrated that Vpr_{HIV-1} engages UNG2 by mimicking the DNA phosphate backbone. More precisely, UNG2 residues, which project into the major groove of its endogenous DNA substrate, insert into a hydrophobic cleft formed by Vpr_{HIV-1} Helices-1, -2 and the N-terminal half of Helix-3 [54]. This mechanism might rationalise Vpr_{HIV-1}'s extraordinary binding promiscuity, since the list of potential Vpr_{HIV-1} degradation substrates is significantly enriched in DNA- and RNA-binding proteins [27]. Moreover, promiscuous Vpr_{HIV-1}-induced degradation of host factors with DNA- or RNA-binding activity has been proposed to induce cell cycle arrest at the G2/M phase border, which is the most thoroughly described phenotype of Vpr proteins so far [26, 27, 61]. In Vpr_{mus}, the N-terminal half of Helix-1 as well as the bulky amino acid residue W48, which is also conserved in Vpr_{agm} and Vpx, constrict the hydrophobic cleft (S6A, B Fig). Furthermore, the extended N-terminus of Vpr_{mus} Helix-3 is not compatible with UNG2-binding due to steric exclusion (S6C Fig). In accordance with these observations, Vpr_{mus} does not down-regulate UNG2 in a human T cell line [27]. However, Vpr_{mus}, Vpr_{syk} and Vpr_{agm} also cause G2/M cell cycle arrest in their respective host cells [60, 62, 63]. This strongly hints at the existence of further structural determinants in Vpr_{mus}, Vpr_{syk}, Vpr_{agm} and potentially Vpr_{HIV-1}, which regulate recruitment and ubiquitylation of DNA/RNA-binding host factors, in addition to the hydrophobic, DNA-mimicking cleft on top of the three-helix bundle. Future efforts to structurally characterise these determinants will further extend our understanding of how the Vpx/Vpr helical scaffold binds, and in this way adapts to a multitude of *neo*-substrate epitopes. In addition, such efforts might inform approaches to design novel $CRL4^{DCAF1}$-based synthetic degraders, in the form of proteolysis-targeting chimera-(PROTAC-) type compounds [64, 65].

Our cryo-EM reconstructions of $CRL4^{DCAF1\text{-}CtD}$/Vpr_{mus}/SAMHD1, complemented by CLMS, also provide insights into the structural dynamics of CRL4 assemblies prior to ubiquitin transfer. The data confirm previously described rotational movement of the CRL4 stalk, in the absence of constraints imposed by a crystal lattice, creating a ubiquitylation zone around the Vpr_{mus}-modified substrate receptor (Figs 5 and 6A) [13, 15, 16, 19, 58]. Missing density for the neddylated CUL4 WHB domain and for the catalytic ROC1 RING domain indicates that these distal stalk elements are highly mobile and likely sample a multitude of orientations relative to the CUL4 scaffold (Fig 6B). These observations are in line

with structure analyses of CRL1 and CRL5, where CUL1/5 neddylation leads to re-orientation of the cullin WHB domain, and to release of the ROC1 RING domain from the cullin scaffold, concomitant with stimulation of ubiquitylation activity [57]. Moreover, recent cryo-EM structure analysis of $CRL1^{\beta\text{-}TRCP}$/IκBα demonstrated substantial mobility of pre-catalytic NEDD8-CUL1 WHB and ROC1 RING domains [66]. Such flexibility seems necessary to structurally organise multiple CRL1-dependent processes, in particular the nucleation of a catalytic assembly, involving intricate protein-protein interactions between NEDD8, CUL1, ubiquitin-charged E2 and substrate receptor. This synergistic assembly then steers the ubiquitin C-terminus towards a substrate lysine for priming with ubiquitin [66]. Accordingly, our cryo-EM studies might indicate that similar principles apply for CRL4-catalysed ubiquitylation. However, to unravel the catalytic architecture of CRL4, sophisticated cross-linking procedures as in reference (65) will have to be pursued.

Intrinsic mobility of CRL4 stalk elements might assist the accommodation of a variety of sizes and shapes of substrates in the CRL4 ubiquitylation zone and might rationalise the wide substrate range accessible to CRL4 ubiquitylation through multiple DCAF receptors. Owing to selective pressure to counteract the host's SAMHD1 restriction, HIV-2 and certain SIVs, amongst other viruses, have taken advantage of this dynamic CRL4 architecture by modification of the DCAF1 substrate receptor with Vpx/Vpr-family accessory proteins. By tethering either SAMHD1-CtD or -NtD to DCAF1, and in this way flexibly recruiting the bulk of SAMHD1, the accessibility of lysine side chains both tether-proximal and on the SAMHD1 globular domains to the CRL4 catalytic assembly might be further improved (Fig 6C, D). This ensures efficient Vpx/Vpr-mediated SAMHD1 priming, poly-ubiquitylation and proteasomal degradation to stimulate virus replication.

Methods

Protein expression and purification

Constructs were PCR-amplified from cDNA templates and inserted into the indicated expression plasmids using standard restriction enzyme methods (S2 Table). pAcGHLT-B-DDB1 (plasmid #48638) and pET28-UBA1 (plasmid #32534) were obtained from Addgene. The pOPC-UBA3-GST-APPBP1 co-expression plasmid, and the pGex6P2-UBC12 plasmid were obtained from MRC-PPU Reagents and

Services (clones 32498, 3879). Bovine erythrocyte ubiquitin and recombinant hsNEDD8 were purchased from Sigma-Aldrich (U6253) and BostonBiochem (UL-812) respectively. Point mutations were introduced by site-directed mutagenesis using KOD polymerase (Novagen). All constructs and variants are summarised S3 Table.

Proteins expressed from vectors pAcGHLT-B, pGex6P1/2, pOPC and pET49b contained an N-terminal GST-His-tag; pHisSUMO – N-terminal His-SUMO-tag; pET28, pRSF-Duet-1 – N-terminal His-tag; pTri-Ex-6 – C-terminal His-tag. Constructs in vectors pAcGHLT-B and pTri-Ex-6 were expressed in Sf9 cells, and constructs in vectors pET28, pET49b, pGex6P1/2, pRSF-Duet-1, and pHisSUMO in *E. coli* Rosetta 2(DE3).

Recombinant baculoviruses (*Autographa californica nucleopolyhedrovirus* clone C6) were generated as described previously [67]. Sf9 cells were cultured in Insect-XPRESS medium (Lonza) at 28°C in an Innova 42R incubator shaker (New Brunswick) at a shaking speed of 180 rpm. In a typical preparation, 1 L of Sf9 cells at 3×10^6 cells/mL were co-infected with 4 mL of high titre DDB1 virus and 4 mL of high titre DCAF1-CtD virus for 72 h.

For a typical *E. coli* Rosetta 2 (DE3) expression, 2 L of LB medium was inoculated with 20 mL of an overnight culture and grown in a Multitron HT incubator shaker (Infors) at 37°C, 150 rpm until OD_{600} reached 0.7. At that point, temperature was reduced to 18°C, protein expression was induced by addition of 0.2 mM IPTG, and cultures were grown for further 20 h. During co-expression of CUL4 and ROC1 from pRSF-Duet, 50 μM zinc sulfate was added to the growth medium before induction.

Sf9 cells were pelleted by centrifugation at 1000 rpm, 4°C for 30 min using a JLA 9.1000 centrifuge rotor (Beckman). *E. coli* cells were pelleted by centrifugation at 4000 rpm, 4°C for 15 min using the same rotor. Cell pellets were resuspended in buffer containing 50 mM Tris, pH 7.8, 500 mM NaCl, 4 mM MgCl2, 0.5 mM tris-(2-carboxyethyl)-phosphine (TCEP), mini-complete protease inhibitors (1 tablet per 50 mL) and 20 mM imidazole (for His-tagged proteins only). 100 mL of lysis buffer was used for resuspension of a pellet from 1 L Sf9 culture, and 35 mL lysis buffer per pellet from 1 L *E. coli* culture. Before resuspension of CUL4/ROC1 co-expression pellets, the buffer pH was adjusted to 8.5. 5 μL Benzonase (Merck) was added and the cells lysed by passing the suspension at least twice through a Microfluidiser (Microfluidics). Lysates were clarified by centrifugation at 48000xg for 45 min at 4°C.

Protein purification was performed at 4°C on an Äkta pure FPLC (GE) using XK 16/20 chromatography columns (GE) containing 10 mL of the appropriate affinity resin. GST-tagged proteins were captured on glutathione-Sepharose (GSH-Sepharose FF, GE), washed with 250 mL of wash buffer (50 mM Tris-HCl pH 7.8, 500 mM NaCl, 4 mM $MgCl_2$, 0.5 mM TCEP), and eluted with the same buffer supplemented with 20 mM reduced glutathione. His-tagged proteins were immobilised on Ni-Sepharose HP (GE), washed with 250 mL of wash buffer supplemented with 20 mM imidazole, and eluted with wash buffer containing 0.3 M imidazole. Eluent fractions were analysed by SDS-PAGE, and appropriate fractions were pooled and reduced to 5 mL using centrifugal filter devices (Vivaspin). If applicable, 100 µg GST-3C protease, or 50 µg thrombin, per mg total protein, was added and the sample was incubated for 12 h on ice to cleave off affinity tags. As second purification step, gel filtration chromatography (GF) was performed on an Äkta prime plus FPLC (GE), with Superdex 200 16/600 columns (GE), equilibrated in 10 mM Tris-HCl pH 7.8, 150 mM NaCl, 4 mM $MgCl_2$, 0.5 mM TCEP buffer, at a flow rate of 1 mL/min. For purification of the CUL4/ROC1 complex, the pH of all purification buffers was adjusted to 8.5. Peak fractions were analysed by SDS-PAGE, appropriate fractions were pooled and concentrated to approx. 20 mg/mL, flash-frozen in liquid nitrogen in small aliquots and stored at -80°C. Protein concentrations were determined with a NanoDrop spectrophotometer (ND 1000, Peqlab), using theoretical absorption coefficients calculated based upon the amino acid sequence by ProtParam on the ExPASy webserver [68].

Analytical gel filtration analysis

Prior to gel filtration analysis affinity tags were removed by incubation of 30 µg GST-3C protease with 6 µM of each protein component in a volume of 120 µL wash buffer, followed by incubation on ice for 12 h. In order to remove the cleaved GST-tag and GST-3C protease, 20 µL GSH-Sepharose FF beads (GE) were added and the sample was rotated at 4 °C for one hour. GSH-Sepharose beads were removed by centrifugation at 4°C, 3500 rpm for 5 min, and 120 µL of the supernatant was loaded on an analytical GF column (Superdex 200 10/300 GL, GE), equilibrated in 10 mM Tris-HCl pH 7.8, 150 mM NaCl, 4 mM $MgCl_2$, 0.5 mM TCEP, at a flow rate of 0.5 mL/min. 1 mL fractions were collected and analysed by SDS-PAGE.

In vitro ubiquitylation assays

160 µL reactions were prepared, containing 0.5 µM substrate (indicated SAMHD1 constructs, S2 Fig), 0.125 µM DDB1/DCAF1-CtD, 0.125 µM CUL4/ROC1, 0.125 µM HisSUMO-T4L-Vpr_{mus} (residues 1-92), 0.25 µM UBCH5C, 15 µM ubiquitin in 20 mM Tris-HCl pH 7.8, 150 mM NaCl, 2.5 mM $MgCl_2$, 2.5 mM ATP. In control reactions, certain components were left out as indicated in S2 Fig. A 30 µl sample for SDS-PAGE analysis was taken (t=0). Reactions were initiated by addition of 0.05 µM UBA1, incubated at 37°C, and 30 µl SDS-PAGE samples were taken after 1 min, 2 min, 5 min and 15 min, immediately mixed with 10 µl 4x SDS sample buffer and boiled at 95°C for 5 min. Samples were analysed by SDS-PAGE.

In vitro neddylation of CUL4/ROC1

For initial neddylation tests, a 200 µL reaction was prepared, containing 8 µM CUL4/ROC1, 1.8 µM UBC12, 30 µM NEDD8 in 50 mM Tris-HCl pH 7.8, 150 mM NaCl, 2.5 mM $MgCl_2$, 2.5 mM ATP. 2x 30 µL samples were taken for SDS-PAGE, one was immediately mixed with 10 µL 4x SDS sample buffer, the other one incubated for 60 min at 25°C. The reaction was initiated by addition of 0.7 µM APPBP1/UBA3, incubated at 25°C, and 30 µL SDS-PAGE samples were taken after 1 min, 5 min, 10 min, 30 min and 60 min, immediately mixed with 10 µL 4x SDS sample buffer and boiled at 95°C for 5 min. Samples were analysed by SDS-PAGE. Based on this test, the reaction was scaled up to 1 mL and incubated for 5 min at 25°C. Reaction was quenched by addition of 5 mM TCEP and immediately loaded onto a Superdex 200 16/600 GF column (GE), equilibrated in 10 mM Tris-HCl pH 7.8, 150 mM NaCl, 4 mM $MgCl_2$, 0.5 mM TCEP at a flow rate of 1 mL/min. Peak fractions were analysed by SDS-PAGE, appropriate fractions were pooled and concentrated to ~20 mg/mL, flash-frozen in liquid nitrogen in small aliquots and stored at -80°C.

X-ray crystallography sample preparation, crystallisation, data collection and structure solution

DDB1/DCAF1-CtD complex. DDB1/DCAF1-CtD crystals were grown by the hanging drop vapour diffusion method, by mixing equal volumes (1 µL) of DDB1/DCAF1-CtD solution at 10 mg/mL with reservoir solution containing 100 mM Tri-Na citrate pH 5.5, 18% PEG 1000 and suspending over a 500 µl reservoir. Crystals grew over night at 18°C. Crystals were cryo-protected in reservoir solution supplemented with 20% glycerol and cryo-cooled in liquid nitrogen. A data set from a single crystal was collected at Diamond Light Source (Didcot, UK) at a wavelength of 0.92819 Å. Data were processed using XDS [69] (S1 Table), and the structure was solved using molecular replacement with the program MOLREP [70] and available structures of DDB1 (PDB 3e0c) and DCAF1-CtD (PDB 4cc9) [50] as search models. Iterative cycles of model adjustment with the program Coot [71], followed by refinement using the program PHENIX [72] yielded final R/R_{free} factors of 22.0%/27.9% (S1 Table). In the model, 94.5 % of residues have backbone dihedral angles in the favoured region of the Ramachandran plot, the remainder fall in the allowed regions, and none are outliers. Details of data collection and refinement statistics are presented in S1 Table. Coordinates and structure factors have been deposited in the PDB, accession number 6zue.

DDB1/DCAF1-CtD/T4L-Vpr$_{mus}$ (1-92) complex. The DDB1/DCAF1-CtD/Vpr$_{mus}$ complex was assembled by incubation of purified DDB1/DCAF1-CtD and HisSUMO-T4L-Vpr$_{mus}$ (residues 1-92), at a 1:1 molar ratio, in a buffer containing 50 mM Bis-tris propane pH 8.5, 0.5 M NaCl, 4 mM $MgCl_2$, 0.5 mM TCEP, containing 1 mg of HRV-3C protease for HisSUMO-tag removal. After incubation on ice for 12 h, the sample was loaded onto a Superdex 200 16/600 GF column (GE), with a 1 mL GSH-Sepharose FF column (GE) connected in line. The column was equilibrated with 10 mM Bis-tris propane pH 8.5, 150 mM NaCl, 4 mM MgCl2, and 0.5 mM TCEP. The column flow rate was 1 mL/min. GF fractions were analysed by SDS-PAGE, appropriate fractions were pooled and concentrated to 4.5 mg/mL.

Crystals were prepared by the sitting drop vapour diffusion method, by mixing equal volumes (200 nL) of the protein complex at 4.5 mg/mL and reservoir solution containing 8-10% PEG 4000 (w/v), 200 mM $MgCl_2$, 100 mM HEPES-NaOH, pH 7.0-8.2. The reservoir volume was 75 µL. Crystals grew after at least 4 weeks of incubation at 4°C. Crystals were cryo-protected in reservoir solution supplemented with 20% glycerol and cryo-cooled in liquid nitrogen. Data sets from two single crystals were collected,

initially at BESSY II (Helmholtz-Zentrum Berlin, HZB) at a wavelength of 0.91841 Å, and later at ESRF (Grenoble) at a wavelength of 1 Å. Data sets were processed separately using XDS [69] and XDSAPP [73]. The structure was solved by molecular replacement, using the initial BESSY data set, with the program PHASER [74], and the following structures as search models: DDB1/DCAF1-CtD (this work) and T4L variant E11H (PDB 1qt6) [75]. After optimisation of the initial model and refinement against the higher-resolution ESRF data set, Vpr_{mus} was placed manually into the density, using an NMR model of Vpr_{HIV-1} (PDB 1m8l) [76] as guidance. Iterative cycles of model adjustment with the program Coot [71], followed by refinement using the program PHENIX [72] yielded final R/R_{free} factors of 21.61%/26.05%. In the model, 95.1 % of residues have backbone dihedral angles in the favoured region of the Ramachandran plot, the remainder fall in the allowed regions, and none are outliers. Details of data collection and refinement statistics are presented in S1 Table. Coordinates and structure factors have been deposited in the PDB, accession number 6zx9.

Cryo-EM sample preparation and data collection

Complex assembly. Purified CUL4-NEDD8/ROC1, DDB1/DCAF1-CtD, GST-Vpr_{mus} and rhesus macaque SAMHD1, 1 µM each, were incubated in a final volume of 1 mL of 10 mM Tris-HCl pH 7.8, 150 mM NaCl, 4 mM $MgCl_2$, 0.5 mM TCEP, supplemented with 1 mg of GST-3C protease. After incubation on ice for 12 h, the sample was loaded onto a Superdex 200 16/600 GF column (GE), equilibrated with the same buffer at 1 mL/min, with a 1 mL GSH-Sepharose FF column (GE) connected in line. GF fractions were analysed by SDS-PAGE, appropriate fractions were pooled and concentrated to 2.8 mg/mL.

Grid preparation. 3.5 µl protein solution containing 0.05 µM CUL4-NEDD8/ROC1/DDB1/DCAF1-CtD/Vpr_{mus}/SAMHD1 complex and 0.25 µM UBCH5C-ubiquitin conjugate (S4 A, B Fig) were applied to a 300 mesh Quantifoil R2/4 Cu/Rh holey carbon grid (Quantifoil Micro Tools GmbH) coated with an additional thin carbon film as sample support and stained with 2% uranyl acetate for initial characterisation. For cryo-EM, a fresh 400 mesh Quantifoil R1.2/1.3 Cu holey carbon grid (Quantifoil Micro Tools GmbH) was glow-discharged for 30 s using a Harrick plasma cleaner with technical air at 0.3 mbar and 7 W. 3.5 µl protein solution containing 0.4 µM CUL4-NEDD8/ROC1/DDB1/DCAF1-

554 CtD/Vpr$_{mus}$/SAMHD1 complex and 2 µM UBCH5C-ubiquitin conjugate were applied to the grid,
555 incubated for 45 s, blotted with a Vitrobot Mark II device (FEI, Thermo Fisher Scientific) for 1-2 s at
556 8°C and 80% humidity, and plunged in liquid ethane. Grids were stored in liquid nitrogen until imaging.
557 **Cryo-EM data collection.** Initial negative stain and cryo-EM datasets were collected automatically
558 for sample quality control and low-resolution reconstructions on a 120 kV Tecnai Spirit cryo-EM (FEI,
559 Thermo Fisher Scientific) equipped with a F416 CMOS camera (TVIPS) using Leginon [77, 78].
560 Particle images were then analysed by 2D classification and initial model reconstruction using SPHIRE
561 [79], cisTEM [80] and Relion 3.07 [81]. These data revealed the presence of the complexes containing
562 both DDB1/DCAF1-CtD/Vpr$_{mus}$ (core) and CUL4/ROC1 (stalk). High-resolution data was collected on
563 a 300 kV Tecnai Polara cryo-EM (FEI, Thermo Fisher Scientific) equipped with a K2summit direct
564 electron detector (Gatan) at a nominal magnification of 31000x, with a pixel size of 0.625 Å/px on the
565 object scale. In total, 3644 movie stacks were collected in super-resolution mode using Leginon [77, 78]
566 with the following parameters: defocus range of 0.5-3.0 µm, 40 frames per movie, 10 s exposure time,
567 electron dose of 1.25 e/Å^2/s and a cumulative dose of 50 e/Å^2 per movie.
568
569 **Cryo-EM computational analysis**
570 Movies were aligned and dose-weighted using MotionCor2 [82] and initial estimation of the contrast
571 transfer function (CTF) was performed with the CTFFind4 package [83]. Resulting micrographs were
572 manually inspected to exclude images with substantial contaminants (typically large protein aggregates
573 or ice contaminations) or grid artefacts. Power spectra were manually inspected to exclude images with
574 astigmatic, weak, or poorly defined spectra. After these quality control steps the dataset included 2322
575 micrographs (63% of total). At this stage, the data set was picked twice and processed separately, to
576 yield reconstructions of the core (analysis 1) and states-1, -2 and -3 (analysis 2).
577 For **analysis 1**, particle positions were determined using template matching with a filtered map
578 comprising core and stalk using the software Gautomatch (https://www2.mrc-
579 lmb.cam.ac.uk/research/locally-developed-software/zhang-software/). 712,485 particle images were
580 found, extracted with Relion 3.07 and subsequently 2D-classified using cryoSPARC [84], resulting in
581 505,342 particle images after selection (S4C, D Fig). These particle images were separated into two

equally sized subsets and Tier 1 3D-classification was performed using Relion 3.07 on both of them to reduce computational burden (S4D Fig). The following parameters were used: initial model="core", number of classes K=4, T=10, global step search=7.5°, number of iterations=25, pixel size 3.75 Å/px. From these, the ones possessing both core and stalk were selected. Classes depicting a similar stalk orientation relative to the core were pooled and directed into Tier 2 as three different subpopulations containing 143,172, 193,059 and 167,666 particle images, respectively (S4D Fig).

For Tier 2, each subpopulation was classified separately into 4 classes each. From these 12 classes, all particle images exhibiting well-defined densities for core and stalk were pooled and labelled "core+stalk", resulting in 310,801 particle images in total. 193,096 particle images representing classes containing only the core were pooled and labelled "core" (S4D Fig)

For Tier 3, the "core" particle subset was separated into 4 classes which yielded uninterpretable reconstructions lacking medium- or high-resolution features. The "core+stalk" subset was separated into 6 classes, with 5 classes containing both stalk and core (S4D Fig) and one class consisting only of the core with Vpr_{mus} bound. The 5 classes with stalk showed similar stalk orientations as the ones obtained from analysis 2 (see below, S5 Fig), but refined individually to lower resolution as in analysis 2 and were discarded. However, individual refinement of the core-only tier 3 class yielded a 7.3 Å reconstruction (S4E, F Fig).

For **analysis 2**, particle positions were determined using cisTEMs Gaussian picking routine, yielding 959,155 particle images in total. After two rounds of 2D-classification, 227,529 particle images were selected for further processing (S4G, H Fig). Using this data, an initial model was created using Relion 3.07. The resulting map yielded strong signal for the core but only fragmented stalk density, indicating a large heterogeneity in the stalk-region within the data set. This large degree of compositional (+/- stalk) and conformational heterogeneity (movement of the stalk relative to the core) made the classification challenging. Accordingly, alignment and classification were carried out simultaneously. The first objective was to separate the data set into three categories: "junk", "core" and "core+stalk". Therefore, the stalk was deleted from the initial model using the "Eraser"-tool in Chimera [85]. This core-map was used as an initial model for the Tier 1 3D-classification with Relion 3.07 at a decimated pixel size of 2.5 Å/px. The following parameters were used: number of classes K=6, T=10, global step

search=7.5°, number of iterations= 25. The classification yielded two classes containing the stalk (classes 3 and 5 containing 23% and 22% of the particle images, respectively) (S4H Fig). These particles were pooled and directed into Tier 2 3D-classification using the following parameters: number of classes K=6, T=10, global step search=7.5°, number of iterations=25. Three of these classes yielded medium-resolution maps with interpretable features (states-1, -2 and -3, S4H Fig). These three classes were refined individually using 3D Relion 3.07, resulting in maps with resolution ranging from 7.8 Å – 8.9 Å (S4H-J Fig).

Molecular visualisation, rigid body fitting, 3D structural alignments, rotation and interface analysis

Density maps and atomic models were visualised using Coot [71], PyMOL (Schrödinger) and UCSF Chimera [85]. Rigid body fits and structural alignments were performed using the program UCSF Chimera [85]. Rotation angles between extreme DDB1 BPB domain positions were measured using the DynDom server [86] (http://dyndom.cmp.uea.ac.uk/dyndom/runDyndom.jsp). Molecular interfaces were analysed using the EBI PDBePISA server [87] (https://www.ebi.ac.uk/msd-srv/prot_int/cgi-bin/piserver).

Multiple sequence alignment

A multiple sequence alignment was calculated using the EBI ClustalOmega server [88] (https://www.ebi.ac.uk/Tools/msa/clustalo/), and adjusted manually using the program GeneDoc [89].

Cross-linking mass spectrometry (CLMS)

Complex assembly. Purified CUL4/ROC1, DDB1/DCAF1-CtD, GST-Vpr_{mus} and rhesus macaque SAMHD1, 1 µM each, were incubated in a volume of 3 mL buffer containing 10 mM HEPES pH 7.8, 150 mM NaCl, 4 mM $MgCl_2$, 0.5 mM TCEP, supplemented with 1 mg GST-3C protease. After incubation on ice for 12 h, the sample was loaded onto a Superdex 200 16/600 GF column (GE), equilibrated with the same buffer, at a flow rate of 1 mL/min with a 1 mL GSH-Sepharose FF column

(GE) connected in line. GF fractions were analysed by SDS-PAGE, appropriate fractions were pooled and concentrated to 6 mg/mL.

Photo-Crosslinking. The cross-linker sulfo-SDA (sulfosuccinimidyl 4,4′-azipentanoate) (Thermo Scientific) was dissolved in cross-linking buffer (10 mM HEPES pH 7.8, 150 mM NaCl, 4 mM $MgCl_2$, 0.5 mM TCEP) to 100 mM before use. The labelling step was performed by incubating 18 µg aliquots of the complex at 1 mg/mL with 2, 1, 0.5, 0.25, 0.125 mM sulfo-SDA, added, respectively, for an hour. The samples were then irradiated with UV light at 365 nm, to form cross-links, for 20 min and quenched with 50 mM NH_4HCO_3 for 20 min. All steps were performed on ice. Reaction products were separated on a Novex Bis-Tris 4–12% SDS−PAGE gel (Life Technologies). The gel band corresponding to the cross-linked complex was excised and digested with trypsin (Thermo Scientific Pierce) [90] and the resulting tryptic peptides were extracted and desalted using C18 StageTips [91]. Eluted peptides were fractionated on a Superdex Peptide 3.2/300 increase column (GE Healthcare) at a flow rate of 10 µL/min using 30% (v/v) acetonitrile and 0.1 % (v/v) trifluoroacetic acid as mobile phase. 50 µL fractions were collected and vacuum-dried.

CLMS acquisition. Samples for analysis were resuspended in 0.1% (v/v) formic acid, 3.2% (v/v) acetonitrile. LC-MS/MS analysis was performed on an Orbitrap Fusion Lumos Tribrid mass spectrometer (Thermo Fisher) coupled on-line with an Ultimate 3000 RSLCnano HPLC system (Dionex, Thermo Fisher). Samples were separated on a 50 cm EASY-Spray column (Thermo Fisher). Mobile phase A consisted of 0.1% (v/v) formic acid and mobile phase B of 80% (v/v) acetonitrile with 0.1% (v/v) formic acid. Flow rates were 0.3 µL/min using gradients optimized for each chromatographic fraction from offline fractionation, ranging from 2% mobile phase B to 55% mobile phase B over 90 min. MS data were acquired in data-dependent mode using the top-speed setting with a 3 s cycle time. For every cycle, the full scan mass spectrum was recorded using the Orbitrap at a resolution of 120,000 in the range of 400 to 1,500 m/z. Ions with a precursor charge state between 3+ and 7+ were isolated and fragmented. Analyte fragmentation was achieved by Higher-Energy Collisional Dissociation (HCD) [92] and fragmentation spectra were then recorded in the Orbitrap with a resolution of 50,000. Dynamic exclusion was enabled with single repeat count and 60 s exclusion duration.

CLMS processing. A recalibration of the precursor m/z was conducted based on high-confidence (<1% false discovery rate (FDR)) linear peptide identifications. The re-calibrated peak lists were searched against the sequences and the reversed sequences (as decoys) of cross-linked peptides using the Xi software suite (v.1.7.5.1) for identification [93]. Final crosslink lists were compiled using the identified candidates filtered to <1% FDR on link level with xiFDR v.2.0 [94] imposing a minimum of 20% sequence coverage and 4 observed fragments per peptide.

CLMS analysis. In order to sample the accessible interaction volume of the SAMHD1-CtD consistent with CLMS data, a model for SAMHD1 was generated using I-TASSER [95]. The SAMHD1-CtD, which adopted a random coil configuration, was extracted from the model. In order to map all crosslinks, missing loops in the complex structure were generated using MODELLER [96]. An interaction volume search was then submitted to the DisVis webserver [97] with an allowed distance between 1.5 Å and 22 Å for each restraint using the "complete scanning" option. The rotational sampling interval was set to 9.72° and the grid voxel spacing to 1Å. The accessible interaction volume was visualised using UCSF Chimera [85].

Acknowledgments

We thank the MPI-MG for granting access to the TEM instruments of the microscopy and cryo-EM service group. We thank Manfred Weiss and the scientific staff of the BESSY-MX (Macromolecular X-ray Crystallography)/Helmholtz Zentrum Berlin für Materialien und Energie at beamlines BL14.1, BL14.2, and BL14.3 operated by the Joint Berlin MX-Laboratory at the BESSY II electron storage ring (Berlin-Adlershof, Germany) as well as the scientific staff of the ESRF (Grenoble, France) at beamlines ID30A-3, ID30B, ID23-1, ID23-2, and ID29 for continuous support. We acknowledge Diamond Light Source (Didcot, UK) for access and support of the synchrotron beamline I04 and cryo-EM facilities at the UK's national Electron Bio-imaging Centre (eBIC). Furthermore, the authors acknowledge the North-German Supercomputing Alliance (HLRN) and the HPC for Research cluster of the Berlin Institute of Health for providing HPC resources. The pHisSUMO plasmid was a generous gift from Dr. Evangelos Christodoulou (The Francis Crick Institute, UK). The rhesus macaque SAMHD1 cDNA template was a generous gift from Prof. Michael Emerman (Fred Hutchinson Cancer Research Center,

692 Seattle, USA). Recombinant BAC10:1629KO bacmid was a generous gift from Prof. Ian Jones
693 (University of Reading, UK). pAcGHLT-B-DDB1 was a gift from Ning Zheng (Addgene plasmid
694 48638). pET28-mE1 was a gift from Jorge Eduardo Azevedo (Addgene plasmid 32534).
695

696 ## Data availability

697 The coordinates and structure factors for the crystal structures have been deposited at the Protein Data
698 Bank (PDB) with the accession codes 6ZUE (DDB1/DCAF1-CtD) and 6ZX9 (DDB1/DCAF1-
699 CtD/T4L-Vpr_{mus} 1-92). Cryo-EM reconstructions have been deposited at the Electron Microscopy Data
700 Bank (EMDB) with the accession codes EMD-10611 (core), EMD-10612 (conformational state-1),
701 EMD-10613 (state-2) and EMD-10614 (state-3). CLMS data have been deposited at the PRIDE database
702 [98] with the accession code PXD020453, reviewer password fCrQG2u8.

References

1. Randow F, Lehner PJ. Viral avoidance and exploitation of the ubiquitin system. Nat Cell Biol. 2009;11(5):527-34. doi: 10.1038/ncb0509-527.

2. Isaacson MK, Ploegh HL. Ubiquitination, ubiquitin-like modifiers, and deubiquitination in viral infection. Cell host & microbe. 2009;5(6):559-70. doi: 10.1016/j.chom.2009.05.012.

3. Gustin JK, Moses AV, Fruh K, Douglas JL. Viral takeover of the host ubiquitin system. Front Microbiol. 2011;2:161. doi: 10.3389/fmicb.2011.00161.

4. Barry M, Fruh K. Viral modulators of cullin RING ubiquitin ligases: culling the host defense. Science's STKE : signal transduction knowledge environment. 2006;2006(335):pe21. Epub 2006/05/18. doi: 10.1126/stke.3352006pe21.

5. Mahon C, Krogan NJ, Craik CS, Pick E. Cullin E3 ligases and their rewiring by viral factors. Biomolecules. 2014;4(4):897-930. Epub 2014/10/15. doi: 10.3390/biom4040897.

6. Becker T, Le-Trilling VTK, Trilling M. Cellular Cullin RING Ubiquitin Ligases: Druggable Host Dependency Factors of Cytomegaloviruses. Int J Mol Sci. 2019;20(7). doi: 10.3390/ijms20071636.

7. Seissler T, Marquet R, Paillart JC. Hijacking of the Ubiquitin/Proteasome Pathway by the HIV Auxiliary Proteins. Viruses. 2017;9(11). doi: 10.3390/v9110322.

8. Zheng N, Shabek N. Ubiquitin Ligases: Structure, Function, and Regulation. Annu Rev Biochem. 2017;86:14.1-29.

9. Sauter D, Kirchhoff F. Key Viral Adaptations Preceding the AIDS Pandemic. Cell host & microbe. 2019;25(1):27-38. doi: 10.1016/j.chom.2018.12.002.

10. Sharp PM, Hahn BH. Origins of HIV and the AIDS pandemic. Cold Spring Harbor perspectives in medicine. 2011;1(1):a006841. Epub 2012/01/10. doi: 10.1101/cshperspect.a006841.

11. Hatziioannou T, Del Prete GQ, Keele BF, Estes JD, McNatt MW, Bitzegeio J, et al. HIV-1-induced AIDS in monkeys. Science. 2014;344(6190):1401-5. Epub 2014/06/21. doi: 10.1126/science.1250761.

12. Malim MH, Bieniasz PD. HIV Restriction Factors and Mechanisms of Evasion. Cold Spring Harbor perspectives in medicine. 2012;2(5):a006940. Epub 2012/05/04. doi: 10.1101/cshperspect.a006940.

13. Fischer ES, Scrima A, Bohm K, Matsumoto S, Lingaraju GM, Faty M, et al. The molecular basis of CRL4DDB2/CSA ubiquitin ligase architecture, targeting, and activation. Cell. 2011;147(5):1024-39. Epub 2011/11/29. doi: 10.1016/j.cell.2011.10.035.

14. Lee J, Zhou P. DCAFs, the missing link of the CUL4-DDB1 ubiquitin ligase. Molecular cell. 2007;26(6):775-80. Epub 2007/06/26. doi: 10.1016/j.molcel.2007.06.001.

15. Angers S, Li T, Yi X, MacCoss MJ, Moon RT, Zheng N. Molecular architecture and assembly of the DDB1-CUL4A ubiquitin ligase machinery. Nature. 2006;443(7111):590-3. Epub 2006/09/12. doi: 10.1038/nature05175.

16. Scrima A, Konickova R, Czyzewski BK, Kawasaki Y, Jeffrey PD, Groisman R, et al. Structural basis of UV DNA-damage recognition by the DDB1-DDB2 complex. Cell. 2008;135(7):1213-23. Epub 2008/12/27. doi: 10.1016/j.cell.2008.10.045.

17. Zimmerman ES, Schulman BA, Zheng N. Structural assembly of cullin-RING ubiquitin ligase complexes. Current opinion in structural biology. 2010;20(6):714-21. Epub 2010/10/01. doi: 10.1016/j.sbi.2010.08.010.

18. Andrejeva J, Young DF, Goodbourn S, Randall RE. Degradation of STAT1 and STAT2 by the V proteins of simian virus 5 and human parainfluenza virus type 2, respectively: consequences for virus replication in the presence of alpha/beta and gamma interferons. Journal of virology. 2002;76(5):2159-67. doi: 10.1128/jvi.76.5.2159-2167.2002.

19. Li T, Chen X, Garbutt KC, Zhou P, Zheng N. Structure of DDB1 in complex with a paramyxovirus V protein: viral hijack of a propeller cluster in ubiquitin ligase. Cell. 2006;124(1):105-17. Epub 2006/01/18. doi: 10.1016/j.cell.2005.10.033.

20. Trilling M, Le VT, Fiedler M, Zimmermann A, Bleifuss E, Hengel H. Identification of DNA-damage DNA-binding protein 1 as a conditional essential factor for cytomegalovirus replication in interferon-gamma-stimulated cells. PLoS pathogens. 2011;7(6):e1002069. doi: 10.1371/journal.ppat.1002069.

21. Paradkar PN, Duchemin JB, Rodriguez-Andres J, Trinidad L, Walker PJ. Cullin4 Is Pro-Viral during West Nile Virus Infection of Culex Mosquitoes. PLoS pathogens. 2015;11(9):e1005143. doi: 10.1371/journal.ppat.1005143.

22. Decorsiere A, Mueller H, van Breugel PC, Abdul F, Gerossier L, Beran RK, et al. Hepatitis B virus X protein identifies the Smc5/6 complex as a host restriction factor. Nature. 2016;531(7594):386-9. doi: 10.1038/nature17170.

23. Murphy CM, Xu Y, Li F, Nio K, Reszka-Blanco N, Li X, et al. Hepatitis B Virus X Protein Promotes Degradation of SMC5/6 to Enhance HBV Replication. Cell reports. 2016;16(11):2846-54. doi: 10.1016/j.celrep.2016.08.026.

762 24. Lim ES, Fregoso OI, McCoy CO, Matsen FA, Malik HS, Emerman M. The ability of primate
763 lentiviruses to degrade the monocyte restriction factor SAMHD1 preceded the birth of the viral accessory protein
764 Vpx. Cell host & microbe. 2012;11(2):194-204. Epub 2012/01/31. doi: 10.1016/j.chom.2012.01.004.
765 25. Romani B, Cohen EA. Lentivirus Vpr and Vpx accessory proteins usurp the cullin4-DDB1 (DCAF1)
766 E3 ubiquitin ligase. Current opinion in virology. 2012;2(6):755-63. Epub 2012/10/16. doi:
767 10.1016/j.coviro.2012.09.010.
768 26. Fabryova H, Strebel K. Vpr and Its Cellular Interaction Partners: R We There Yet? Cells. 2019;8(11).
769 doi: 10.3390/cells8111310.
770 27. Greenwood EJD, Williamson JC, Sienkiewicz A, Naamati A, Matheson NJ, Lehner PJ. Promiscuous
771 Targeting of Cellular Proteins by Vpr Drives Systems-Level Proteomic Remodeling in HIV-1 Infection. Cell
772 reports. 2019;27(5):1579-96 e7. doi: 10.1016/j.celrep.2019.04.025.
773 28. Schrofelbauer B, Yu Q, Zeitlin SG, Landau NR. Human immunodeficiency virus type 1 Vpr induces the
774 degradation of the UNG and SMUG uracil-DNA glycosylases. Journal of virology. 2005;79(17):10978-87. doi:
775 10.1128/JVI.79.17.10978-10987.2005.
776 29. Lahouassa H, Blondot ML, Chauveau L, Chougui G, Morel M, Leduc M, et al. HIV-1 Vpr degrades the
777 HLTF DNA translocase in T cells and macrophages. Proceedings of the National Academy of Sciences of the
778 United States of America. 2016;113(19):5311-6. doi: 10.1073/pnas.1600485113.
779 30. Laguette N, Bregnard C, Hue P, Basbous J, Yatim A, Larroque M, et al. Premature activation of the
780 SLX4 complex by Vpr promotes G2/M arrest and escape from innate immune sensing. Cell. 2014;156(1-2):134-
781 45. Epub 2014/01/15. doi: 10.1016/j.cell.2013.12.011.
782 31. Zhou X, DeLucia M, Ahn J. SLX4-SLX1 Protein-independent Down-regulation of MUS81-EME1
783 Protein by HIV-1 Viral Protein R (Vpr). The Journal of biological chemistry. 2016;291(33):16936-47. doi:
784 10.1074/jbc.M116.721183.
785 32. Romani B, Shaykh Baygloo N, Aghasadeghi MR, Allahbakhshi E. HIV-1 Vpr Protein Enhances
786 Proteasomal Degradation of MCM10 DNA Replication Factor through the Cul4-DDB1[VprBP] E3 Ubiquitin
787 Ligase to Induce G2/M Cell Cycle Arrest. The Journal of biological chemistry. 2015;290(28):17380-9. doi:
788 10.1074/jbc.M115.641522.
789 33. Lv L, Wang Q, Xu Y, Tsao LC, Nakagawa T, Guo H, et al. Vpr Targets TET2 for Degradation by
790 CRL4(VprBP) E3 Ligase to Sustain IL-6 Expression and Enhance HIV-1 Replication. Molecular cell.
791 2018;70(5):961-70 e5. doi: 10.1016/j.molcel.2018.05.007.

792 34. Su J, Rui Y, Lou M, Yin L, Xiong H, Zhou Z, et al. HIV-2/SIV Vpx targets a novel functional domain
793 of STING to selectively inhibit cGAS-STING-mediated NF-kappaB signalling. Nat Microbiol. 2019;4(12):2552-
794 64. doi: 10.1038/s41564-019-0585-4.
795 35. Chougui G, Munir-Matloob S, Matkovic R, Martin MM, Morel M, Lahouassa H, et al. HIV-2/SIV viral
796 protein X counteracts HUSH repressor complex. Nat Microbiol. 2018;3(8):891-7. doi: 10.1038/s41564-018-
797 0179-6.
798 36. Yurkovetskiy L, Guney MH, Kim K, Goh SL, McCauley S, Dauphin A, et al. Primate
799 immunodeficiency virus proteins Vpx and Vpr counteract transcriptional repression of proviruses by the HUSH
800 complex. Nat Microbiol. 2018;3(12):1354-61. doi: 10.1038/s41564-018-0256-x.
801 37. Hrecka K, Hao C, Gierszewska M, Swanson SK, Kesik-Brodacka M, Srivastava S, et al. Vpx relieves
802 inhibition of HIV-1 infection of macrophages mediated by the SAMHD1 protein. Nature. 2011;474(7353):658-
803 61. Epub 2011/07/02. doi: 10.1038/nature10195.
804 38. Laguette N, Sobhian B, Casartelli N, Ringeard M, Chable-Bessia C, Segeral E, et al. SAMHD1 is the
805 dendritic- and myeloid-cell-specific HIV-1 restriction factor counteracted by Vpx. Nature. 2011;474(7353):654-
806 7. Epub 2011/05/27. doi: 10.1038/nature10117.
807 39. Powell RD, Holland PJ, Hollis T, Perrino FW. Aicardi-Goutieres syndrome gene and HIV-1 restriction
808 factor SAMHD1 is a dGTP-regulated deoxynucleotide triphosphohydrolase. The Journal of biological chemistry.
809 2011;286(51):43596-600. Epub 2011/11/10. doi: 10.1074/jbc.C111.317628.
810 40. Goldstone DC, Ennis-Adeniran V, Hedden JJ, Groom HC, Rice GI, Christodoulou E, et al. HIV-1
811 restriction factor SAMHD1 is a deoxynucleoside triphosphate triphosphohydrolase. Nature.
812 2011;480(7377):379-82. Epub 2011/11/08. doi: 10.1038/nature10623.
813 41. Zhu C, Gao W, Zhao K, Qin X, Zhang Y, Peng X, et al. Structural insight into dGTP-dependent
814 activation of tetrameric SAMHD1 deoxynucleoside triphosphate triphosphohydrolase. Nature communications.
815 2013;4:2722. Epub 2013/11/13. doi: 10.1038/ncomms3722.
816 42. Kim B, Nguyen LA, Daddacha W, Hollenbaugh JA. Tight interplay among SAMHD1 protein level,
817 cellular dNTP levels, and HIV-1 proviral DNA synthesis kinetics in human primary monocyte-derived
818 macrophages. The Journal of biological chemistry. 2012;287(26):21570-4. Epub 2012/05/17. doi:
819 10.1074/jbc.C112.374843.
820 43. Lahouassa H, Daddacha W, Hofmann H, Ayinde D, Logue EC, Dragin L, et al. SAMHD1 restricts the
821 replication of human immunodeficiency virus type 1 by depleting the intracellular pool of deoxynucleoside
822 triphosphates. Nature immunology. 2012;13(3):223-8. Epub 2012/02/14. doi: 10.1038/ni.2236.

823 44. St Gelais C, de Silva S, Amie SM, Coleman CM, Hoy H, Hollenbaugh JA, et al. SAMHD1 restricts
824 HIV-1 infection in dendritic cells (DCs) by dNTP depletion, but its expression in DCs and primary CD4+ T-
825 lymphocytes cannot be upregulated by interferons. Retrovirology. 2012;9:105. Epub 2012/12/13. doi:
826 10.1186/1742-4690-9-105.
827 45. Rehwinkel J, Maelfait J, Bridgeman A, Rigby R, Hayward B, Liberatore RA, et al. SAMHD1-
828 dependent retroviral control and escape in mice. The EMBO journal. 2013;32(18):2454-62. Epub 2013/07/23.
829 doi: 10.1038/emboj.2013.163.
830 46. Morris ER, Taylor IA. The missing link: allostery and catalysis in the anti-viral protein SAMHD1.
831 Biochem Soc Trans. 2019;47(4):1013-27. doi: 10.1042/BST20180348.
832 47. Baldauf HM, Pan X, Erikson E, Schmidt S, Daddacha W, Burggraf M, et al. SAMHD1 restricts HIV-1
833 infection in resting CD4(+) T cells. Nature medicine. 2012;18(11):1682-7. Epub 2012/09/14. doi:
834 10.1038/nm.2964.
835 48. Shingai M, Welbourn S, Brenchley JM, Acharya P, Miyagi E, Plishka RJ, et al. The Expression of
836 Functional Vpx during Pathogenic SIVmac Infections of Rhesus Macaques Suppresses SAMHD1 in CD4+
837 Memory T Cells. PLoS pathogens. 2015;11(5):e1004928. doi: 10.1371/journal.ppat.1004928.
838 49. Fregoso OI, Ahn J, Wang C, Mehrens J, Skowronski J, Emerman M. Evolutionary toggling of Vpx/Vpr
839 specificity results in divergent recognition of the restriction factor SAMHD1. PLoS pathogens.
840 2013;9(7):e1003496. Epub 2013/07/23. doi: 10.1371/journal.ppat.1003496.
841 50. Schwefel D, Groom HC, Boucherit VC, Christodoulou E, Walker PA, Stoye JP, et al. Structural basis of
842 lentiviral subversion of a cellular protein degradation pathway. Nature. 2014;505(7482):234-8. Epub 2013/12/18.
843 doi: 10.1038/nature12815.
844 51. Schwefel D, Boucherit VC, Christodoulou E, Walker PA, Stoye JP, Bishop KN, et al. Molecular
845 Determinants for Recognition of Divergent SAMHD1 Proteins by the Lentiviral Accessory Protein Vpx. Cell
846 host & microbe. 2015;17(4):489-99. Epub 2015/04/10. doi: 10.1016/j.chom.2015.03.004.
847 52. Wu Y, Koharudin LM, Mehrens J, DeLucia M, Byeon CH, Byeon IJ, et al. Structural Basis of Clade-
848 specific Engagement of SAMHD1 (Sterile alpha Motif and Histidine/Aspartate-containing Protein 1) Restriction
849 Factors by Lentiviral Viral Protein X (Vpx) Virulence Factors. The Journal of biological chemistry.
850 2015;290(29):17935-45. doi: 10.1074/jbc.M115.665513.
851 53. Spragg CJ, Emerman M. Antagonism of SAMHD1 is actively maintained in natural infections of simian
852 immunodeficiency virus. Proceedings of the National Academy of Sciences of the United States of America.
853 2013;110(52):21136-41. Epub 2013/12/11. doi: 10.1073/pnas.1316839110.

54. Wu Y, Zhou X, Barnes CO, DeLucia M, Cohen AE, Gronenborn AM, et al. The DDB1-DCAF1-Vpr-UNG2 crystal structure reveals how HIV-1 Vpr steers human UNG2 toward destruction. Nature structural & molecular biology. 2016;23(10):933-40. doi: 10.1038/nsmb.3284.

55. Enchev RI, Schulman BA, Peter M. Protein neddylation: beyond cullin-RING ligases. Nature reviews Molecular cell biology. 2015;16(1):30-44. doi: 10.1038/nrm3919.

56. Schneider M, Belsom A, Rappsilber J. Protein Tertiary Structure by Crosslinking/Mass Spectrometry. Trends in biochemical sciences. 2018;43(3):157-69. Epub 2018/02/06. doi: 10.1016/j.tibs.2017.12.006.

57. Duda DM, Borg LA, Scott DC, Hunt HW, Hammel M, Schulman BA. Structural insights into NEDD8 activation of cullin-RING ligases: conformational control of conjugation. Cell. 2008;134(6):995-1006. doi: 10.1016/j.cell.2008.07.022.

58. Fischer ES, Bohm K, Lydeard JR, Yang H, Stadler MB, Cavadini S, et al. Structure of the DDB1-CRBN E3 ubiquitin ligase in complex with thalidomide. Nature. 2014;512(7512):49-53. doi: 10.1038/nature13527.

59. DeLucia M, Mehrens J, Wu Y, Ahn J. HIV-2 and SIVmac accessory virulence factor Vpx down-regulates SAMHD1 enzyme catalysis prior to proteasome-dependent degradation. The Journal of biological chemistry. 2013;288(26):19116-26. doi: 10.1074/jbc.M113.469007.

60. Berger G, Lawrence M, Hue S, Neil SJ. G2/M cell cycle arrest correlates with primate lentiviral Vpr interaction with the SLX4 complex. Journal of virology. 2014. Epub 2014/10/17. doi: 10.1128/JVI.02307-14.

61. Guenzel CA, Herate C, Benichou S. HIV-1 Vpr-a still "enigmatic multitasker". Front Microbiol. 2014;5:127. doi: 10.3389/fmicb.2014.00127.

62. Stivahtis GL, Soares MA, Vodicka MA, Hahn BH, Emerman M. Conservation and host specificity of Vpr-mediated cell cycle arrest suggest a fundamental role in primate lentivirus evolution and biology. Journal of virology. 1997;71(6):4331-8.

63. Planelles V, Jowett JB, Li QX, Xie Y, Hahn B, Chen IS. Vpr-induced cell cycle arrest is conserved among primate lentiviruses. Journal of virology. 1996;70(4):2516-24.

64. Schapira M, Calabrese MF, Bullock AN, Crews CM. Targeted protein degradation: expanding the toolbox. Nat Rev Drug Discov. 2019;18(12):949-63. doi: 10.1038/s41573-019-0047-y.

65. Hanzl A, Winter GE. Targeted protein degradation: current and future challenges. Curr Opin Chem Biol. 2020;56:35-41. doi: 10.1016/j.cbpa.2019.11.012.

883 66. Baek K, Krist DT, Prabu JR, Hill S, Klugel M, Neumaier LM, et al. NEDD8 nucleates a multivalent
884 cullin-RING-UBE2D ubiquitin ligation assembly. Nature. 2020;578(7795):461-6. doi: 10.1038/s41586-020-
885 2000-y.
886 67. Zhao Y, Chapman DA, Jones IM. Improving baculovirus recombination. Nucleic acids research.
887 2003;31(2):E6-. Epub 2003/01/16.
888 68. Wilkins MR, Gasteiger E, Bairoch A, Sanchez JC, Williams KL, Appel RD, et al. Protein identification
889 and analysis tools in the ExPASy server. Methods Mol Biol. 1999;112:531-52. Epub 1999/02/23. doi: 10.1385/1-
890 59259-584-7:531.
891 69. Kabsch W. Xds. Acta crystallographica Section D, Biological crystallography. 2010;66(Pt 2):125-32.
892 Epub 2010/02/04. doi: 10.1107/S0907444909047337.
893 70. Vagin A, Teplyakov A. Molecular replacement with MOLREP. Acta crystallographica Section D,
894 Biological crystallography. 2010;66(Pt 1):22-5. Epub 2010/01/09. doi: 10.1107/S0907444909042589.
895 71. Emsley P, Cowtan K. Coot: model-building tools for molecular graphics. Acta crystallographica Section
896 D, Biological crystallography. 2004;60(Pt 12 Pt 1):2126-32. Epub 2004/12/02. doi:
897 10.1107/S0907444904019158.
898 72. Liebschner D, Afonine PV, Baker ML, Bunkoczi G, Chen VB, Croll TI, et al. Macromolecular structure
899 determination using X-rays, neutrons and electrons: recent developments in Phenix. Acta Crystallogr D Struct
900 Biol. 2019;75(Pt 10):861-77. Epub 2019/10/08. doi: 10.1107/S2059798319011471.
901 73. Sparta KM, Krug M, Heinemann U, Mueller U, Weiss MS. XDSAPP2.0. Journal of Applied
902 Crystallography. 2016;49(3):1085-92. doi: doi:10.1107/S1600576716004416.
903 74. McCoy AJ, Grosse-Kunstleve RW, Adams PD, Winn MD, Storoni LC, Read RJ. Phaser
904 crystallographic software. Journal of Applied Crystallography. 2007;40(4):658-74. doi:
905 doi:10.1107/S0021889807021206.
906 75. Kuroki R, Weaver LH, Matthews BW. Structural basis of the conversion of T4 lysozyme into a
907 transglycosidase by reengineering the active site. Proceedings of the National Academy of Sciences of the
908 United States of America. 1999;96(16):8949-54. Epub 1999/08/04. doi: 10.1073/pnas.96.16.8949.
909 76. Morellet N, Bouaziz S, Petitjean P, Roques BP. NMR structure of the HIV-1 regulatory protein VPR.
910 Journal of molecular biology. 2003;327(1):215-27. Epub 2003/03/05.
911 77. Carragher B, Kisseberth N, Kriegman D, Milligan RA, Potter CS, Pulokas J, et al. Leginon: an
912 automated system for acquisition of images from vitreous ice specimens. J Struct Biol. 2000;132(1):33-45. Epub
913 2000/12/21. doi: 10.1006/jsbi.2000.4314.

914 78. Suloway C, Pulokas J, Fellmann D, Cheng A, Guerra F, Quispe J, et al. Automated molecular
915 microscopy: the new Leginon system. J Struct Biol. 2005;151(1):41-60. Epub 2005/05/14. doi:
916 10.1016/j.jsb.2005.03.010.
917 79. Moriya T, Saur M, Stabrin M, Merino F, Voicu H, Huang Z, et al. High-resolution Single Particle
918 Analysis from Electron Cryo-microscopy Images Using SPHIRE. J Vis Exp. 2017;(123). Epub 2017/06/02. doi:
919 10.3791/55448.
920 80. Grant T, Rohou A, Grigorieff N. cisTEM, user-friendly software for single-particle image processing.
921 Elife. 2018;7. Epub 2018/03/08. doi: 10.7554/eLife.35383.
922 81. Zivanov J, Nakane T, Forsberg BO, Kimanius D, Hagen WJ, Lindahl E, et al. New tools for automated
923 high-resolution cryo-EM structure determination in RELION-3. Elife. 2018;7. Epub 2018/11/10. doi:
924 10.7554/eLife.42166.
925 82. Zheng SQ, Palovcak E, Armache JP, Verba KA, Cheng Y, Agard DA. MotionCor2: anisotropic
926 correction of beam-induced motion for improved cryo-electron microscopy. Nat Methods. 2017;14(4):331-2.
927 Epub 2017/03/03. doi: 10.1038/nmeth.4193.
928 83. Mindell JA, Grigorieff N. Accurate determination of local defocus and specimen tilt in electron
929 microscopy. J Struct Biol. 2003;142(3):334-47. Epub 2003/06/05. doi: 10.1016/s1047-8477(03)00069-8.
930 84. Punjani A, Rubinstein JL, Fleet DJ, Brubaker MA. cryoSPARC: algorithms for rapid unsupervised
931 cryo-EM structure determination. Nat Methods. 2017;14(3):290-6. Epub 2017/02/07. doi: 10.1038/nmeth.4169.
932 85. Pettersen EF, Goddard TD, Huang CC, Couch GS, Greenblatt DM, Meng EC, et al. UCSF Chimera--a
933 visualization system for exploratory research and analysis. J Comput Chem. 2004;25(13):1605-12. Epub
934 2004/07/21. doi: 10.1002/jcc.20084.
935 86. Hayward S, Lee RA. Improvements in the analysis of domain motions in proteins from conformational
936 change: DynDom version 1.50. J Mol Graph Model. 2002;21(3):181-3. Epub 2002/12/05. doi: 10.1016/s1093-
937 3263(02)00140-7.
938 87. Krissinel E, Henrick K. Inference of macromolecular assemblies from crystalline state. Journal of
939 molecular biology. 2007;372(3):774-97. Epub 2007/08/08. doi: 10.1016/j.jmb.2007.05.022.
940 88. Madeira F, Park YM, Lee J, Buso N, Gur T, Madhusoodanan N, et al. The EMBL-EBI search and
941 sequence analysis tools APIs in 2019. Nucleic acids research. 2019;47(W1):W636-W41. Epub 2019/04/13. doi:
942 10.1093/nar/gkz268.
943 89. Nicholas KB, Nicholas Jr., H. B., Deerfield II., D. W. GeneDoc: Analysis and Visualization of Genetic
944 Variation. embnetnews. 1997;4(2):1-4.

945 90. Shevchenko A, Tomas H, Havlis J, Olsen JV, Mann M. In-gel digestion for mass spectrometric
946 characterization of proteins and proteomes. Nature protocols. 2006;1(6):2856-60. Epub 2007/04/05. doi:
947 10.1038/nprot.2006.468.
948 91. Rappsilber J, Ishihama Y, Mann M. Stop and go extraction tips for matrix-assisted laser
949 desorption/ionization, nanoelectrospray, and LC/MS sample pretreatment in proteomics. Anal Chem.
950 2003;75(3):663-70. Epub 2003/02/15. doi: 10.1021/ac026117i.
951 92. Kolbowski L, Mendes ML, Rappsilber J. Optimizing the Parameters Governing the Fragmentation of
952 Cross-Linked Peptides in a Tribrid Mass Spectrometer. Anal Chem. 2017;89(10):5311-8. Epub 2017/04/14. doi:
953 10.1021/acs.analchem.6b04935.
954 93. Mendes ML, Fischer L, Chen ZA, Barbon M, O'Reilly FJ, Giese SH, et al. An integrated workflow for
955 crosslinking mass spectrometry. Mol Syst Biol. 2019;15(9):e8994. Epub 2019/09/27. doi:
956 10.15252/msb.20198994.
957 94. Fischer L, Rappsilber J. Quirks of Error Estimation in Cross-Linking/Mass Spectrometry. Anal Chem.
958 2017;89(7):3829-33. Epub 2017/03/08. doi: 10.1021/acs.analchem.6b03745.
959 95. Yang J, Zhang Y. Protein Structure and Function Prediction Using I-TASSER. Curr Protoc
960 Bioinformatics. 2015;52:5 8 1-5 8 15. Epub 2015/12/19. doi: 10.1002/0471250953.bi0508s52.
961 96. Webb B, Sali A. Comparative Protein Structure Modeling Using MODELLER. Curr Protoc
962 Bioinformatics. 2016;54:5 6 1-5 6 37. Epub 2016/06/21. doi: 10.1002/cpbi.3.
963 97. van Zundert GC, Trellet M, Schaarschmidt J, Kurkcuoglu Z, David M, Verlato M, et al. The DisVis and
964 PowerFit Web Servers: Explorative and Integrative Modeling of Biomolecular Complexes. Journal of molecular
965 biology. 2017;429(3):399-407. Epub 2016/12/13. doi: 10.1016/j.jmb.2016.11.032.
966 98. Perez-Riverol Y, Csordas A, Bai J, Bernal-Llinares M, Hewapathirana S, Kundu DJ, et al. The PRIDE
967 database and related tools and resources in 2019: improving support for quantification data. Nucleic acids
968 research. 2019;47(D1):D442-D50. Epub 2018/11/06. doi: 10.1093/nar/gky1106.

Figures

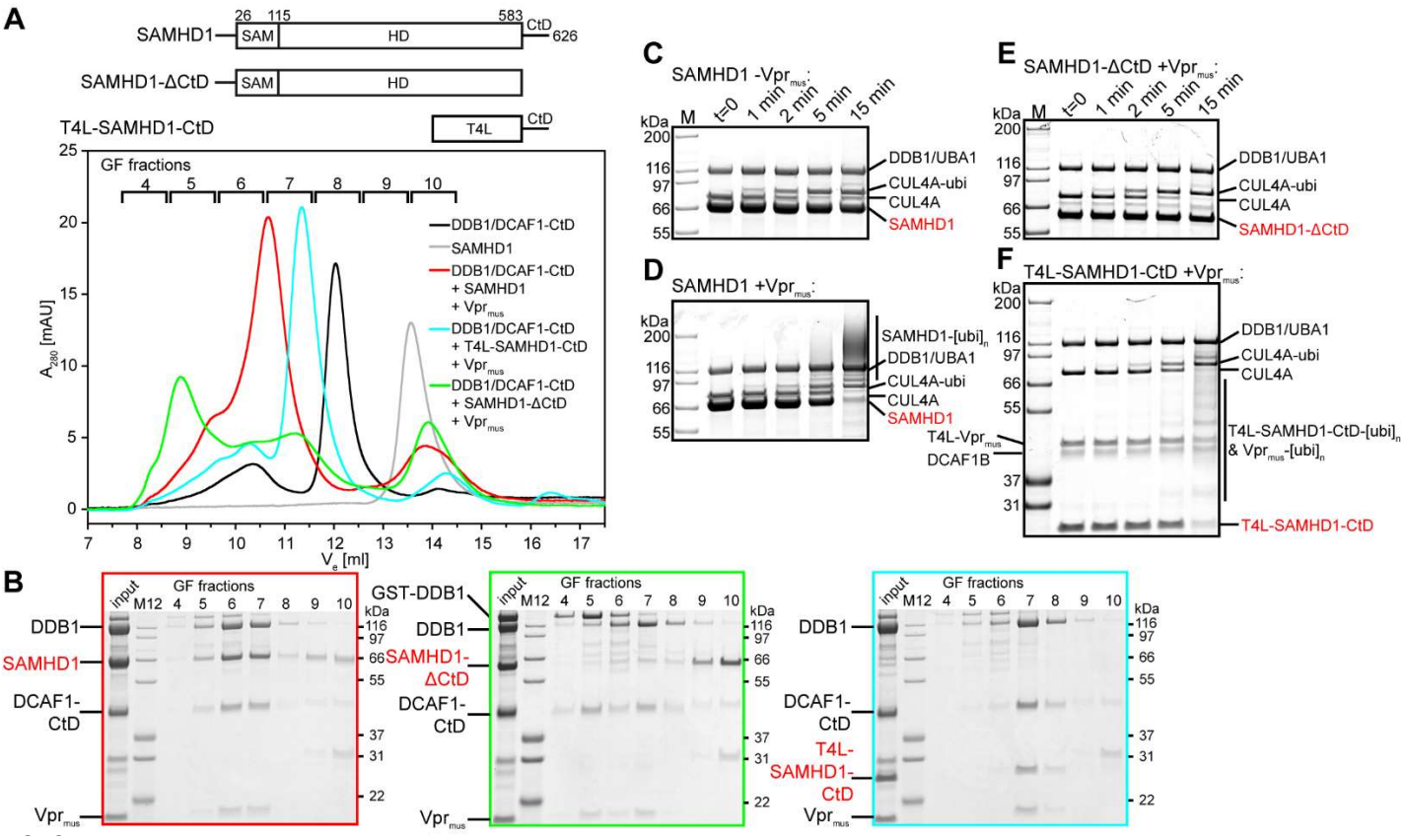

Fig 1. Biochemical analysis of Vpr_{mus}-induced $CRL4^{DCAF1}$ specificity redirection.

(**A**) GF analysis of *in vitro* reconstitution of protein complexes containing DDB1/DCAF1-CtD, Vpr_{mus} and SAMHD1 constructs. A schematic of the SAMHD1 constructs is shown above the chromatograms. SAM – sterile α-motif domain, HD – histidine-aspartate domain, T4L – T4 Lysozyme. (**B**) SDS-PAGE analysis of fractions collected during GF runs in **A**, boxes are colour-coded with respect to the chromatograms. Note that during preparation of the GF run containing SAMHD1-ΔCtD (green trace), the GST-affinity tag, which forms dimers in solution, was not removed completely from DDB1. Accordingly, the GF trace contains an additional dimeric GST-DDB1/DCAF1-CtD/Vpr_{mus} component in fractions 4-5. (**C-F**) *In vitro* ubiquitylation reactions with purified protein components in the absence (**C**) or presence (**D-F**) of Vpr_{mus}, with the indicated SAMHD1 constructs as substrate. Reactions were stopped after the indicated times, separated on SDS-PAGE and visualised by staining.

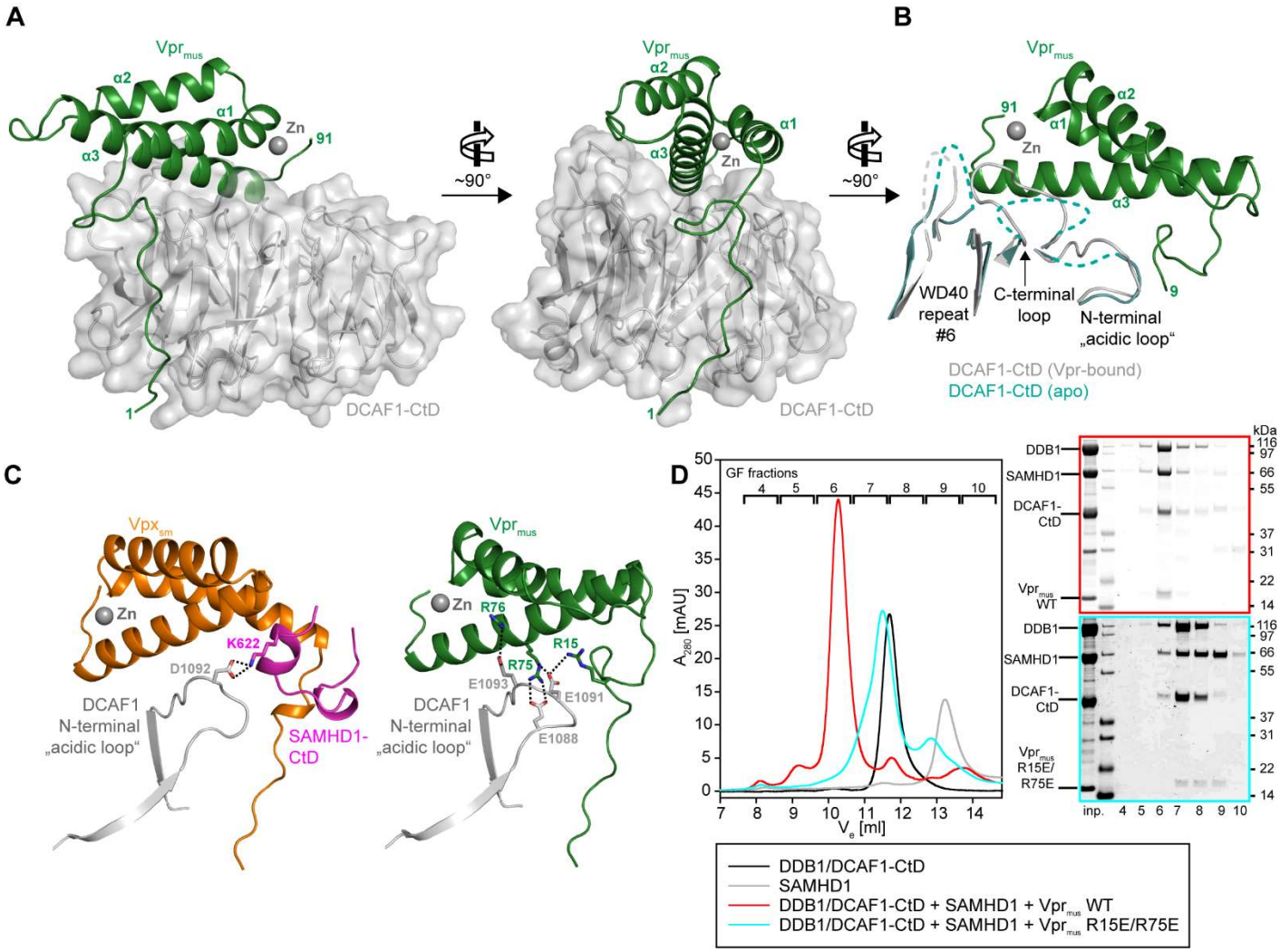

Fig 2. Crystal structure of the DDB1/DCAF1-CtD/Vpr$_{mus}$ complex.

(**A**) Overall structure of the complex in two views. DCAF1-CtD is shown as grey cartoon and semi-transparent surface. Vpr$_{mus}$ is shown as a dark green cartoon with the co-ordinated zinc ion shown as grey sphere. T4L and DDB1 have been omitted for clarity. (**B**) Superposition of apo-DCAF1-CtD (light blue cartoon) with Vpr$_{mus}$-bound DCAF1-CtD (grey/green cartoon). Only DCAF1-CtD regions with significant structural differences between apo- and Vpr$_{mus}$-bound forms are shown. Disordered loops are indicated as dashed lines. (**C**) Comparison of the binary Vpr$_{mus}$/DCAF1-CtD and ternary Vpx$_{sm}$/DCAF1-CtD/SAMHD1-CtD complexes. For DCAF1-CtD, only the N-terminal "acidic loop" region is shown. Vpr$_{mus}$, DCAF1-CtD and bound zinc are coloured as in **A**; Vpx$_{sm}$ is represented as orange cartoon and SAMHD1-CtD as pink cartoon. Selected Vpr/Vpx/DCAF1-CtD side chains are shown as sticks, and electrostatic interactions between these side chains are indicated as dotted lines. (**D**) *In vitro* reconstitution of protein complexes containing DDB1/DCAF1-CtD/Vpr$_{mus}$ or the Vpr$_{mus}$ R15E/R75E

995 mutant, and SAMHD1, analysed by analytical GF. SDS-PAGE analysis of corresponding GF fractions

996 is shown next to the chromatogram.

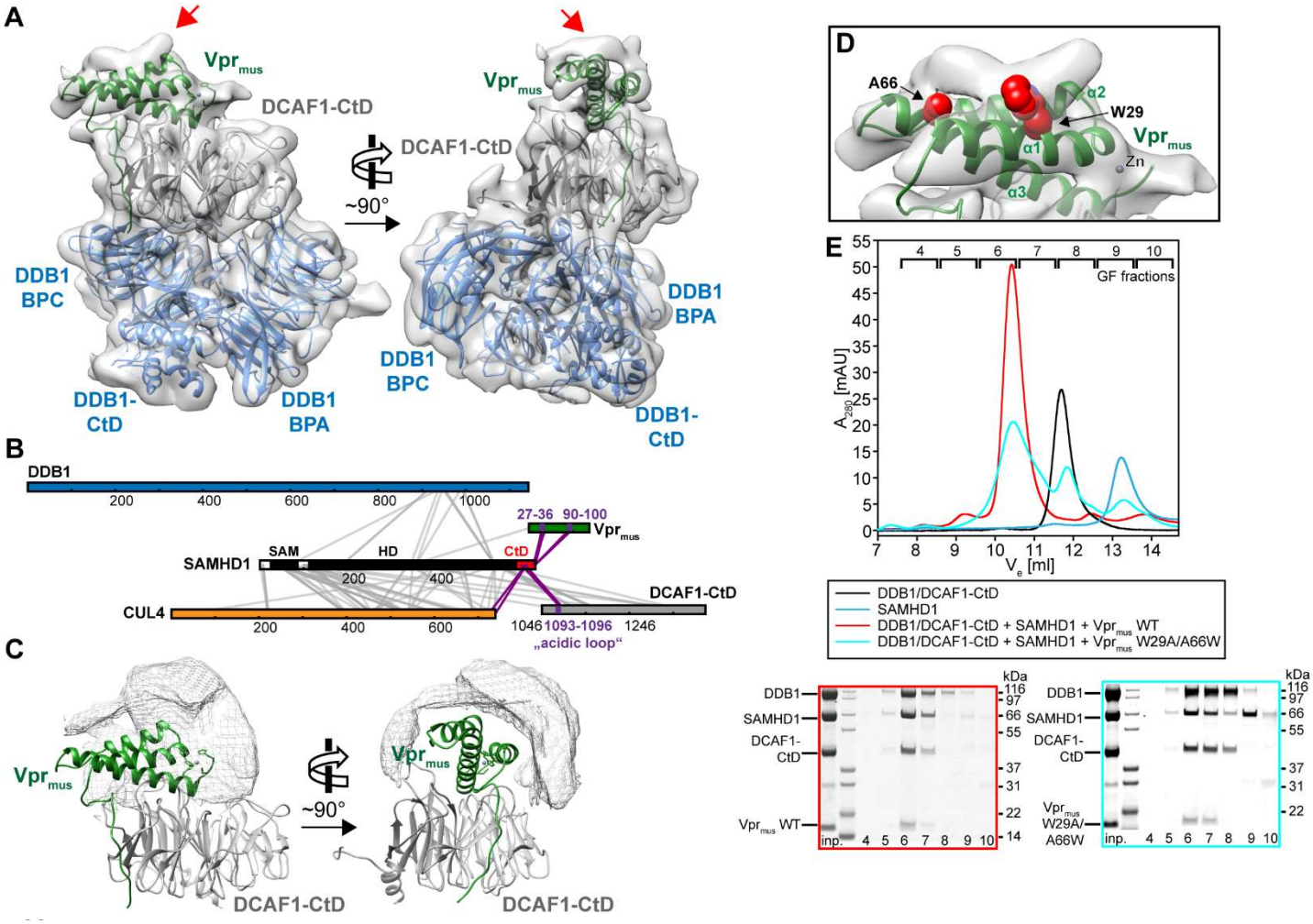

998 **Fig 3. Mechanism of SAMHD1-CtD recruitment by Vpr_{mus}.**

999 (**A**) Two views of the cryo-EM reconstruction of the CRL4-$NEDD8^{DCAF1\text{-}CtD}$/Vpr_{mus}/SAMHD1 core.
1000 The crystal structure of the DDB1/DCAF1-CtD/Vpr_{mus} complex was fitted as a rigid body into the cryo-
1001 EM density and is shown in the same colours as in Fig 2A. The DDB1 BPB model and density was
1002 removed for clarity. The red arrows mark additional density on the upper surface of the Vpr_{mus} helix
1003 bundle. (**B**) Schematic representation of Sulfo-SDA cross-links (grey lines) between $CRL4^{DCAF1}$/Vpr_{mus}
1004 and SAMHD1, identified by CLMS. Proteins are colour-coded as in **A**, CUL4 is coloured orange,
1005 SAMHD1 black/white. SAMHD1-CtD is highlighted in red, and cross-links to SAMHD1-CtD are
1006 highlighted in violet. (**C**) The accessible interaction space of SAMHD1-CtD, calculated by the DisVis
1007 server [97], consistent with at least 14 of 26 observed cross-links, is visualised as grey mesh. DCAF1-
1008 CtD and Vpr_{mus} are oriented and coloured as in **A**. (**D**) Detailed view of the SAMHD1-CtD electron
1009 density. The model is in the same orientation as in **A**, left panel. Selected Vpr_{mus} residues W29 and A66,
1010 which are in close contact to the additional density, are shown as red space-fill representation. (**E**) *In*

vitro reconstitution of protein complexes containing DDB1/DCAF1-CtD, Vpr_{mus} or the Vpr_{mus} W29A/A66W mutant, and SAMHD1, assessed by analytical GF. SDS-PAGE analysis of corresponding GF fractions is shown below the chromatogram.

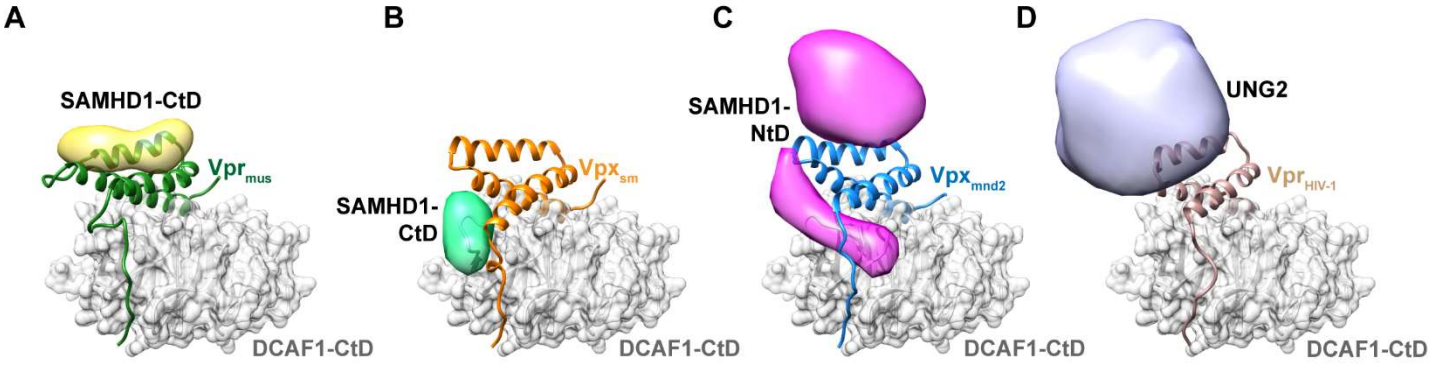

Fig 4. Variability of *neo*-substrate recognition in Vpx/Vpr proteins.

Comparison of *neo*-substrate recognition modes of Vpr_{mus} (**A**), Vpx_{sm} (**B**), Vpx_{mnd2} (**C**) and Vpr_{HIV-1} (**D**) proteins. DCAF1-CtD is shown as grey cartoon and semi-transparent surface, Vpr_{mus} – green, Vpx_{sm} – orange, Vpx_{mnd2} – blue and Vpr_{HIV-1}– light brown are shown as cartoon. Models of the recruited ubiquitylation substrates are shown as strongly filtered, semi-transparent calculated electron density maps with the following colouring scheme: SAMHD1-CtD bound to Vpr_{mus} – yellow, SAMHD1-CtD (bound to Vpx_{sm}, PDB 4cc9) [50] – mint green, SAMHD1-NtD (Vpx_{mnd2}, PDB 5aja) [51] – magenta, UNG2 (Vpr_{HIV-1}, PDB 5jk7) [54] – light violet.

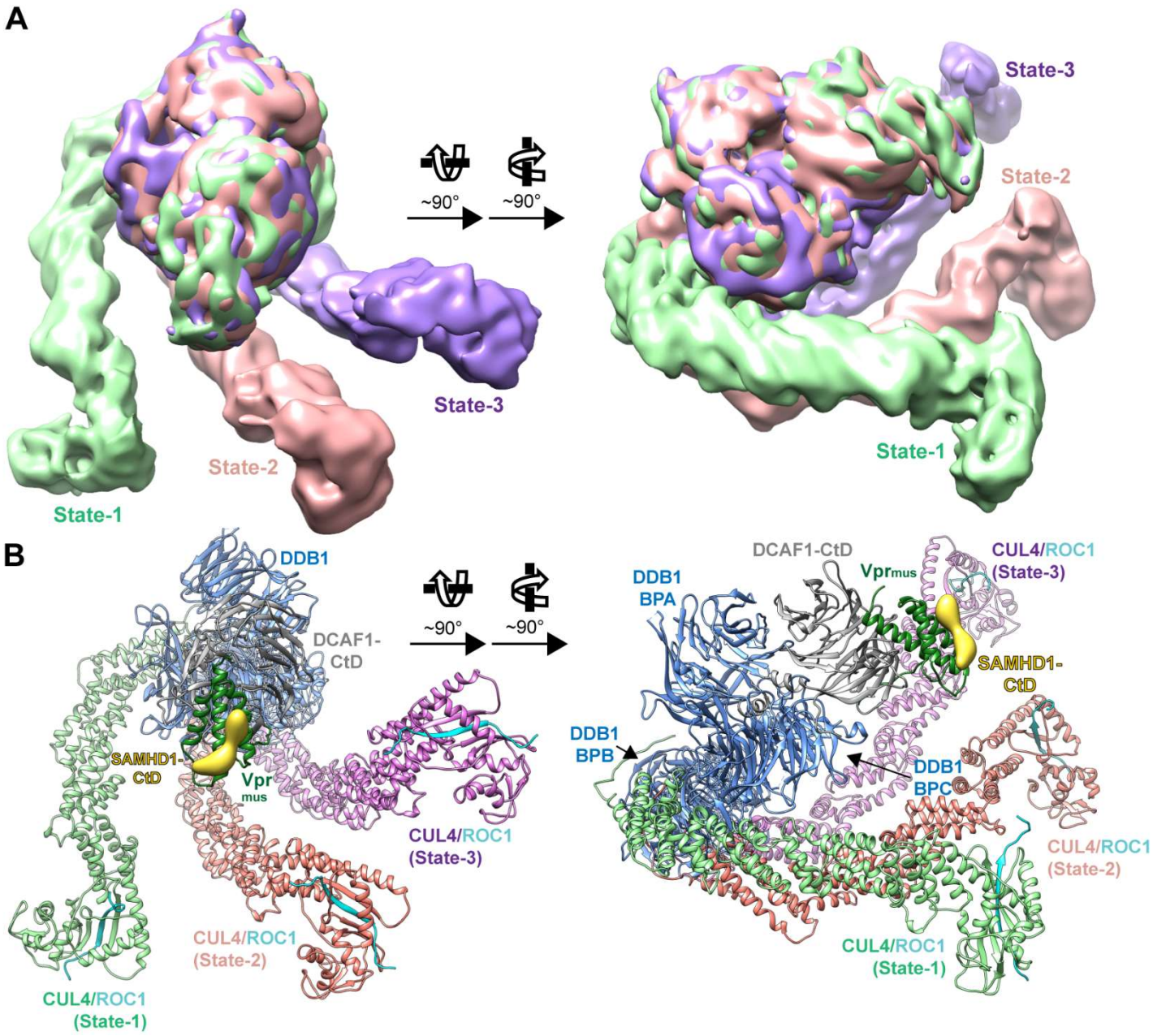

1024 **Fig 5. Cryo-EM analysis of CRL4-NEDD8$^{DCAF1\text{-}CtD}$ conformational states.**

1025 (**A**) Two views of an overlay of CRL4-NEDD8$^{DCAF1\text{-}CtD}$/Vpr$_{mus}$/SAMHD1 cryo-EM reconstructions
1026 (conformational state-1 – light green, state-2 – salmon, state-3 – purple). The portions of the densities
1027 corresponding to DDB1 BPA/BPC, DCAF1-CtD and Vpr$_{mus}$ have been superimposed. (**B**) Two views
1028 of a superposition of DDB1/DCAF1-CtD/Vpr$_{mus}$ and CUL4/ROC1 (PDB 2hye) [15] molecular models,
1029 which have been fitted as rigid bodies to the corresponding cryo-EM densities; the models are oriented
1030 as in **A**. DDB1/DCAF1-CtD/Vpr$_{mus}$ is shown as in Fig 2A, CUL4 is shown as cartoon, coloured as in **A**

and ROC1 is shown as cyan cartoon. Cryo-EM density corresponding to SAMHD1-CtD is shown in yellow, to illustrate the SAMHD1-CtD binding site in the context of the whole CRL4 assembly.

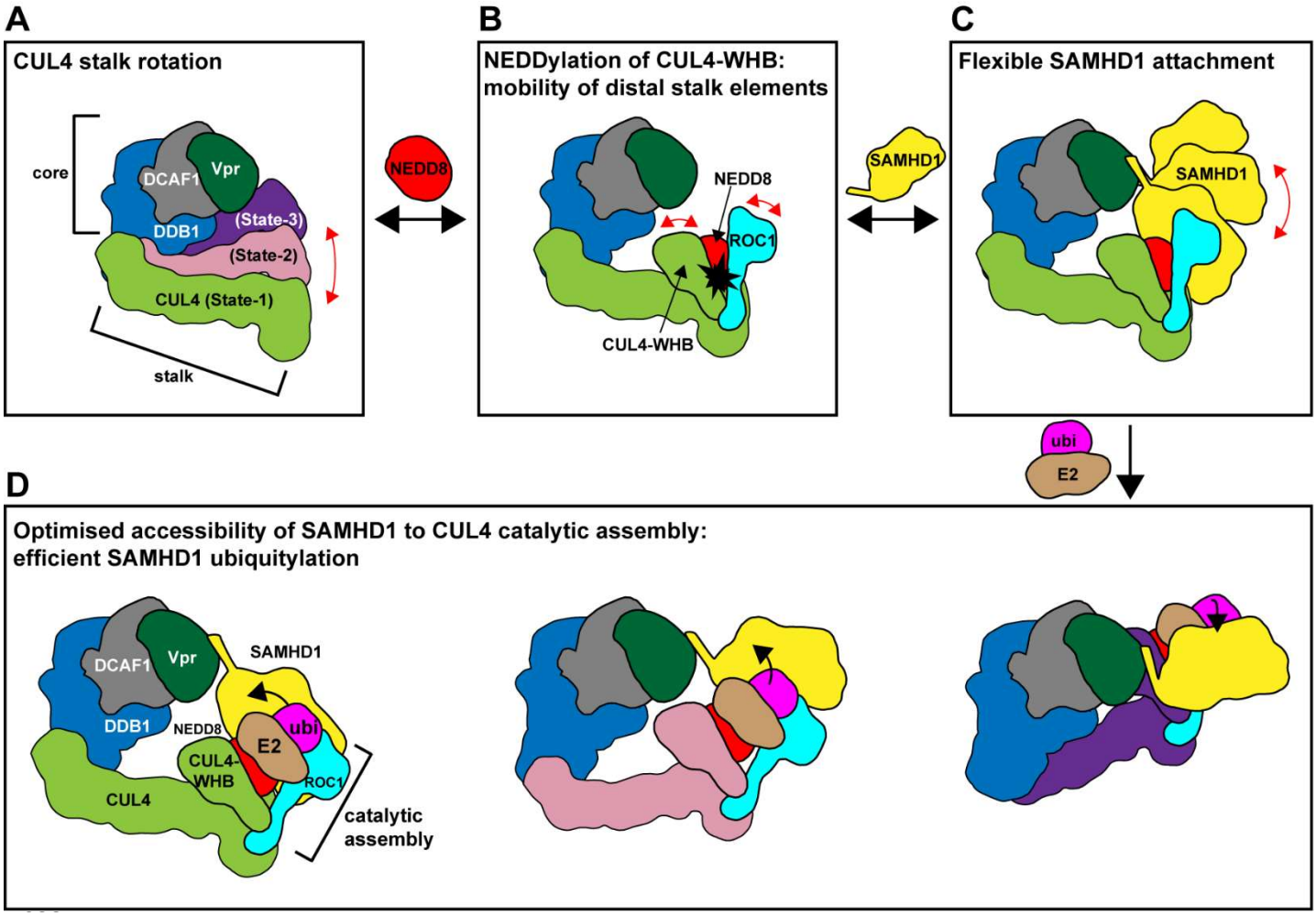

1034 **Fig 6. Schematic illustration of structural plasticity in Vpr$_{mus}$-modified CRL4$^{DCAF1\text{-}CtD}$, and**
1035 **implications for ubiquitin transfer**.

1036 (**A**) Rotation of the CRL4 stalk increases the space accessible to catalytic elements at the distal tip of
1037 the stalk, forming a ubiquitylation zone around the core. (**B**) Modification of CUL4-WHB with NEDD8
1038 leads to increased mobility of these distal stalk elements (CUL4-WHB, ROC1 RING domain) [57],
1039 further extending the ubiquitylation zone and activating the formation of a catalytic assembly for
1040 ubiquitin transfer (see also **D**) [66]. (**C**) Flexible tethering of SAMHD1 to the core by Vpr$_{mus}$ places the
1041 bulk of SAMHD1 in the ubiquitylation zone and optimises surface accessibility. (**D**) Dynamic processes
1042 **A**-**C** together create numerous possibilities for assembly of the catalytic machinery (NEDD8-CUL4-
1043 WHB, ROC1, ubiquitin-(ubi-)charged E2) on surface-exposed SAMHD1 lysine side chains. Here, three
1044 of these possibilities are exemplified schematically. In this way, ubiquitin coverage on SAMHD1 is
1045 maximised.